*Astronomy & Astrophysics* manuscript no. outflows˙Mrk273˙d5
July 24, 2014
© ESO 2014

arXiv:1407.6301v1 [astro-ph.GA] 23 Jul 2014

# Extended Warm Gas in the ULIRG Mrk273: Galactic Outflows and Tidal Debris

J. Rodríguez Zaurín[1,2], C. N. Tadhunter[3], D. S. N. Rupke[4], S. Veilleux[5], H. W. W. Spoon[6], M. Chiaberge[7], C. Ramos Almeida[1,2], D. Batcheldor[8] and W. B. Sparks[7]

[1] Instituto de Astrofísica de Canarias, E-38205, La Laguna, Tenerife, Spain
email: javierr@iac.es
[2] Departamento de Astrofísica, Universidad de La Laguna, Tenerife, Spain
[3] Department of Physics and Astronomy, University of Sheffield, Sheffield S3 7RH
[4] Department of Physics, Rhodes College, Memphis, TN 38112, USA
[5] Department of Astronomy, University of Maryland, College Park, MD 20742, USA
[6] Cornell University, CRSR, Space Sciences Building, Ithaca, NY 14853, USA
[7] Space Telescope Science Institute, 3700 San Martin Drive, Baltimore, MD 21218, USA
[8] Physics and Space Sciences Department, Florida Institute of Technology, 150 West University Boulevard, Melbourne, FL 32901, USA

**ABSTRACT**

We present new *HST* ACS medium- and narrow-band images and long-slit, optical (4000 - 7200Å) spectra obtained using the Isaac Newton Telescope (INT) on La Palma, of the merging system Mrk273. The *HST* observations sample the [OIII]$\lambda\lambda$4959,5007 emission from the galaxy and the nearby continuum. These data were taken as a part of a larger study of ultraluminous infrared galaxies (ULIRGs) with the aim of investigating the importance of the warm, AGN induced outflows in such objects. The *HST* images show that the morphologies of the extended continuum and the ionized gas emission from the galaxy are decoupled, extending almost perpendicular to each other. In particular, we detect for the first time a spectacular structure of ionized gas in the form of filaments and clumps extending ∼23kpc to the east of the nuclear region. The quiescent ionized gas kinematics at these locations suggests that these filaments are tidal debris left over from a secondary merger event that are illuminated by an AGN in the nuclear regions. The images also reveal a complex morphology in the nuclear region of the galaxy for both the continuum and the [OIII] emission. Consistent with this complexity, we find a wide diversity of emission line profiles in these regions. Kinematic disturbance, in the form of broad (FWHM > 500 km s$^{-1}$) and/or strongly shifted ($|\Delta V|$ >150 km s$^{-1}$ ) emission line components, is found at almost all locations in the nuclear regions, but confined to a radius of ∼4 kpc to the east and west of the northern nucleus. In most cases, we are able to fit the profiles of all the emission lines of different ionization with a kinematic model using 2 or 3 Gaussian components. From these fits we derive diagnostic line ratios that are used to investigate the ionization mechanisms at the different locations in the galaxy. We show that, in general, the line ratios are consistent with photoionization by an AGN as the main ionization mechanism. Finally, the highest surface brightness [OIII] emission is found in a compact region that is coincident with the so-called SE nuclear component. The compactness, kinematics and emission line ratios of this component suggest that it is a separate nucleus with its own AGN. At this stage, further observations are required to confirm the dual (or multiple?) AGN nature of Mrk273.

**Key words.** Galaxies: evolution – galaxies: starburst – galaxies:active.

## 1. Introduction

Fast outflows induced by the central QSO are now almost invariably detected in dusty mergers with AGN nuclei (e.g. Westmoquette et al. 2012; Rodríguez Zaurín et al. 2013; Veilleux et al. 2013; Rupke & Veilleux 2013b). These outflows are a key element in simulations of galaxy evolution through major mergers, where they are used to regulate the correlation between the black hole mass and the host galaxy properties (e.g. Silk & Rees 1998; Fabian 1999; Benson et al. 2003; Johansson et al. 2009). In particular, they are predicted to be extremely powerful towards the final stages of the merger, when the merging nuclei coalesce, potentially quenching the surrounding star formation activity (e.g. di Matteo et al. 2005; Springel et al. 2005; Johansson et al. 2009; Hopkins & Elvis 2010). However, from an observational perspective, the nature of their interaction with the ISM in the host galaxies and importance relative to the outflows induced by star formation activity, have yet to be firmly established.

In this context Ultra Luminous Infrared Galaxies (ULIRGs, $L_{IR} > 10^{12}$ $L_{\odot}$) are ideal objects to investigate the physical processes involved in AGN-induced outflows. Their prodigious far-IR radiation represents the dust reprocessed light of nuclear power sources (starbursts and/or AGN). In addition, ULIRGs almost invariably show morphological evidence consistent with triggering of the activity in major galaxy mergers (e.g. Murphy et al. 1996; Clements et al. 1996; Sanders & Mirabel 1996; Surace et al. 2000; Surace & Sanders 2000; Scoville et al. 2000; Veilleux

*Send offprint requests to*: Javier Rodríguez Zaurín
javierr@iac.es

et al. 2002). Therefore, ULIRGs represent just the situation modelled in many of the most recent hydrodynamic simulations.

As expected from the merger simulations, AGN-induced outflows in ULIRGs have recently been found in all gas phases: neutral (Rupke & Veilleux 2011, 2013b), ionized (e.g. Westmoquette et al. 2012; Rodríguez Zaurín et al. 2013; Rupke & Veilleux 2013b) and molecular (e.g. Fischer et al. 2010; Feruglio et al. 2010; Sturm et al. 2011; Veilleux et al. 2013; Cicone et al. 2012, 2013; Rupke & Veilleux 2013a; Spoon et al. 2013). For the ionized and neutral gas, the outflows in ULIRGs with AGN show velocity widths (FWHM) and shifts of up to 1700 km $s^{-1}$ and 2000 km $s^{-1}$ respectively[1] (Rodríguez Zaurín et al. 2013; Rupke & Veilleux 2013b, hereafter RZ13 and RV13). These numbers are substantially smaller for ULIRGs with no detected AGN activity (FWHM typically less than 500 km $s^{-1}$, RV13, RZ13). In the molecular phase, the CO emission and/or OH absorption lines show velocity shifts of up to 1000 km/s in some ULIRGs with AGN activity (Sturm et al. 2011; Veilleux et al. 2013; Cicone et al. 2013). As in the cases of the ionized and neutral phases, the velocity shifts are smaller for those ULIRGs powered by starburst (e.g. Veilleux et al. 2013; Cicone et al. 2013).

Recent integral field spectroscopic (IFS) studies of local samples of ULIRGs have been used to investigate not only the kinematics, but also the spatial structures and the geometries of these outflows (e.g. Colina et al. 1999; Bedregal et al. 2009; Westmoquette et al. 2012, RV13). For example, RV13 found a variety of outflow morphologies, from collimated bipolar winds, sometimes in the form of "super-bubbles", to less collimated shocks extendeding on kiloparsecs scales in the galaxies. However, these studies are usually concentrated in the central few kiloparsecs of the objects, and therefore, it is possible that they do not sample the full extent of the outflowing material. In addition, IFS data are usually limited to a relatively narrow wavelength range, making it hard to determine the ionization mechanism responsible for the outflows. Due to these limitations, the mass outflow rates and kinetic powers derived from these studies remain uncertain.

As one of the closest ULIRGs, Mrk273 (z = 0.0373, $L_{IR}$ = $10^{12.21}$ $L_{\odot}$) represents a key target for studies aimed at understanding the nature of ULIRGs and their associated outflows. This late-merger system shows an impressive tidal tail extending over 40 kpc to the south of the nuclear region. It has been studied extensively at all wavelengths, from the UV to the X-rays (e.g. Condon et al. 1991; Soifer et al. 2000; Armus et al. 2007; Howell et al. 2010; Rodríguez Zaurín et al. 2010; Iwasawa et al. 2011; U et al. 2013). At near- and mid-IR wavelengths, two nuclei become apparent, commonly referred to as northern (N) and south-western (SW) components (Majewski et al. 1993; Knapen et al. 1997; Scoville et al. 2000; Soifer et al. 2000). An additional third nuclear structure, referred to as south eastern (SE) component, emerges at radio wavelengths (Condon et al. 1991). The N nucleus is the strongest radio source (Carilli & Taylor 2000; Bondi et al. 2005) and makes the main contribution to the MIR emission (Soifer et al. 2000). Radio and CO(2–1) observations suggest that the N nucleus is the site of the dense molecular gas disk of $1 \times 10^9$ $M_{\odot}$ containing a compact, powerful starburst formed by several luminous supernovae or supernovae remnants (Condon et al. 1991; Carilli & Taylor 2000; Bondi et al. 2005). However, based on their recent AO IFS near-IR observations of the sources, U et al. (2013) found evidence for a super-massive black hole of mass (1.04±0.1)x$10^9$ solar masses in the N nucleus. In addition, the detection of enhanced Fe K emission at the same location, suggests that this nucleus might contain a heavily obscured AGN (Iwasawa et al. 2011).

The SW component coincides with the location of the hard X-ray point source, and is identified as the host of the AGN (Iwasawa et al. 2011). On the other hand, although the SE component was first identified as a star cluster based on NICMOS images, the strength of the [SiVI] at this location suggests that this region is at least partially ionized by an AGN, with the ionizing AGN perhaps located in the N or SW nucleus (U et al. 2013).

The dominant power source responsible for the IR luminosity of Mrk273 remains uncertain. While the strong [O IV] and [Ne V] emission relative to [Ne II] suggest heating by an AGN as the dominant mechanism (Genzel et al. 1998; Veilleux et al. 2009), the L(MIR)/L(FIR) ratio is consistent with starburst activity powering almost the entire IR luminosity of the source (Veilleux et al. 2009). In addition, other diagnostics based on the equivalent width of the PAH feature at 7.7$\mu$m suggest that the contributions to the heating of the dust by the AGN and starburst components are actually similar (Veilleux et al. 2009).

The nuclear kinematics of the source have been investigated in the past using IFS techniques (Colina et al. 1999, RV13). The RV13 study of the central 4.5 × 6 kpc revealed the presence an "extended" outflow plus a bipolar superbubble, along with a rotating component that traces the CO(1–0) rotation curve of Downes & Solomon (1998). The superbubble is aligned N-S, with projected velocities of up to -1500 km $s^{-1}$, and is likely to be ionized by an AGN.

Although much attention has been paid to the nuclear regions of Mrk273, little work has been done on the morphology, kinematics and ionization of the gas at larger scales. In this paper we present new imaging and spectroscopic observations of Mrk273 taken with the Hubble Space Telescope (*HST*) and the Isaac Newton Telescope (*INT*). We use these combined datasets to relate the properties of the ionized gas emission in the nuclear regions to those on more extended scales. In this way we aim to establish whether the warm, AGN-driven outflows are important for the overall evolution of the host galaxy. Throughout the paper we adopt $H_0$ = 68 km $s^{-1}$, $\Omega_m$ = 0.29 and $\Omega_\Lambda$ = 0.71. At the redshift of the source, this gives a luminosity distance of $D_L$ = 171.5 Mpc and a scale of 0.762 kpc $arcsec^{-1}$.

## 2. Observations and data reduction

### 2.1. Imaging data

#### 2.1.1. *HST* data

New *HST* ACS images of Mrk273 were taken during Cycle 20 as a part of a larger program aimed at studying the AGN-induced outflows in a sample of local ULIRGs (GO:12934, PI:C.N. Tadhunter). The Wide Field Channel (WFC, 0.049 arcsec $pixel^{-1}$) on the ACS was used in combination with the FR505N narrow-band ramp filter, and the

[1] Note that throughout the paper, when we refer to the outflow velocity shifts from the work of Rupke and collaborators, we specifically mean the $v_{50\%}$ values as defined in their papers.

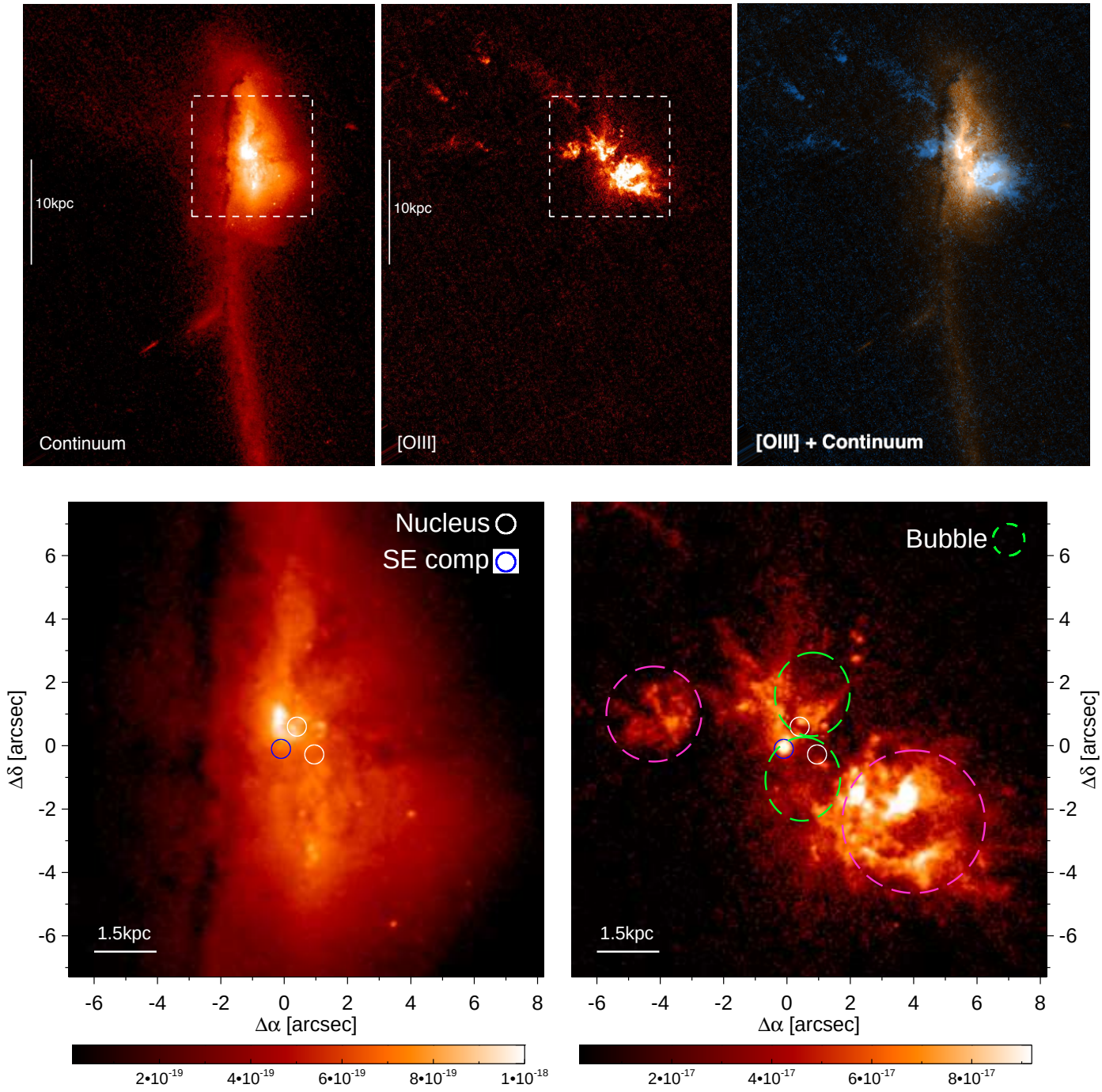


Fig. 1 Upper panel, left to right: *HST*-ACS continuum, continuum subtracted [OIII], and [OIII] (blue)+continuum (red) images of the galaxy. North is up, East is left. The dashed-line boxes indicated the zoomed region in the lower panel. Lower panel: zoom into the central 15×15 arcsec region (11.6×11.6 kpc) for the continuum (upper-left) and the continuum-subtracted [OIII] (upper-middle) images of the galaxy. The color bars at the bottom of the images indicate the flux in units of erg $s^{-1}$ $cm^{-1}$ $Å^{-1}$ and erg $s^{-1}$ $cm^{-1}$ for the continuum and the [OIII] images respectively. The white circles indicate the locations of the N and SW nuclear components observed at IR wavelengths, while the blue circle corresponds to the location of the SE component that emerges at radio wavelengths. The green-dashed line ellipses in the continuum subtracted [OIII] image indicate the location of the nuclear superbubble reported by RV13 in their IFS study of the source, while magenta-dashed line circles indicate the location of the so-called Outflow-East and West (see text for details). A color version of this Figure is available in the online journal.

F550M medium-band filter. The former image was centered on the redshifted [OIII]$\lambda$5007 (hereafter [OIII]) emission line, while the F550M medium-band filter was centered on the nearby continuum towards redder wavelengths. Details of the imaging observations are shown in Table 1.

The data were reduced using the standard data reduction pipeline procedures which employ two packages: the CALACS package, which includes dark subtraction, bias subtraction and flat-field correction and produces calibrated images, and the MULTIDRIZZLE package, which corrects for distortion and performs cosmic ray rejection.

| Telescope | Camera | Filter | $\lambda_c$ (Å) | $\Delta\lambda$ (Å) | Exp time (s) |
|---|---|---|---|---|---|
| *HST* | ACS/WFC | F550M | 5581.5 | 384 | 716 |
| | | FR505N | 5175.6 | 92 | 1356 |
| *INT* | WFC | #228 | 6813 | 93 | 2800 |

Table 1 Log of the imaging observations of Mrk273 (z = 0.0373) used for this paper.

Any remaining cosmic rays were removed manually using the routines IMEDIT in IRAF and/or CLEAN within the STARLINK package FIGARO.

To convert into physical units we used the PHOTFLAM header keyword. PHOTFLAM is the sensitivity conversion factor and is defined as the mean flux density $F_\lambda$ (in units of erg cm$^{-2}$ Å$^{-1}$ counts$^{-1}$) that produces 1 count per second for a given *HST* observing mode. Since drizzled ACS images are in units of counts s$^{-1}$, these may simply be multiplied by the PHOTFLAM value to obtain the flux in units of erg cm$^{-2}$ sec$^{-1}$ Å$^{-1}$. The error associated with the flux calibration, including both the photon noise and calibration uncertainty, is ∼5% for both the continuum and the [OIII] image.

At this stage it is important to add a caveat about the use of the PHOTFLAM parameter. While PHOTFLAM is adequate when the flux is approximately constant through the bandpass, it might not be adequate when the spectrum of the source shows strong emission lines within the bandwidth, which is the case of our [OIII] image. Therefore, to check the accuracy of the calibartion of the *HST* images, we compared them with the Rodríguez Zaurín et al. (2009) WHT-ISIS long slit spectroscopic observations of the source.

To that aim, it is crucial to know the precise location of the slit during the observations. We first convolved the *HST* images with a Gaussian profile to simulate the seeing conditions during the spectrocopic observations. Spatial profiles of width identical to the slit-width of the spectra (1.5 arcsec) were then extracted from the images, in steps of 2 pixels (0.1 arcsec). These spatial profiles were compared with those of spatial slices extracted from the spectra using wavelength ranges selected to match those of the *HST* filters, until a match was found. Following this procedure we were able to find the location of the slits on the image with a precision of 5 *HST* pixels (0.25 arcsec). Once the location of the slit was known, we integrated the emission over the spatial extent of the galaxy covered by the slit for both the *HST* and the *WHT* spatial profiles described before.

The results obtained from this procedure are two flux measurements that can be directly compared to check the consistency between the flux calibrations. If we refer to these flux values as $F_{HST}$ and $F_{WHT}$, we find that $F_{HST}/F_{WHT}$ is equal to 1.05 and 1.10 for the continuum and [OIII] observations respectively. Given the uncertainties associated with the process (e.g. the varying seeing during the spectroscopic observations, or the 5 pixel uncertainty in the slit position) we find that the flux calibrations for the *HST* and the *WHT* observations are in excellent agreement.

Once the images were calibrated in flux we subtracted the continuum from the [OIII] image to end up with an image that traces "pure" [OIII] emission. Prior to this task, it was necessary to align the images. To that aim we used a series of IRAF routines. In the first place we used the task SREGISTER which registers an image to a reference image using celestial coordinate information in the headers. In addition, there are three foreground stars in the ACS/WFC field of view used for the Mrk273 observations. Therefore, it was possible to use the tasks GEOMAP and GEOTRAN to geometrically align the images and refine the final result. The accuracy of the alignment was measured using the routine CENTER that calculates the centroids of the stars in the aligned images. We found that the images are aligned with an accuracy better than 0.02 pixels. The continuum, continuum subtracted, and [OIII]+continuum images are shown in Figure 1.

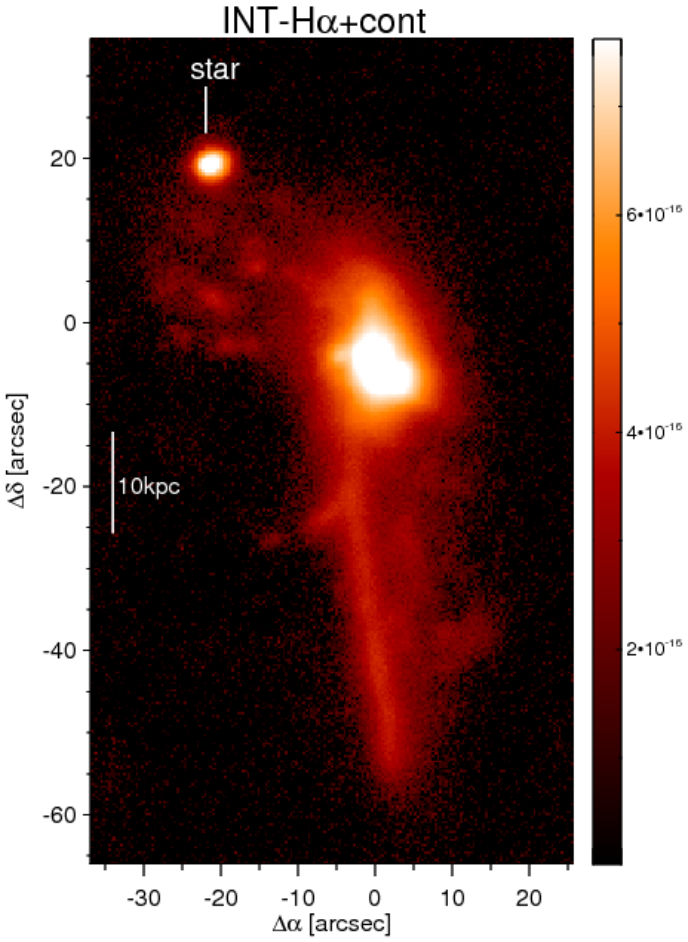


Fig. 2 *INT*-WFC Hα+[NII] image of Mrk273. No continuum emission was subtracted for this image. The color bar to the right of the image indicates the flux in units of ergs s$^{-1}$ cm$^{-2}$. The bright point source to the North-East of the galaxy is a star (a color version of this Figure is available in the online journal).

### 2.1.2. *INT*-WFC data

A deep image of Mrk273 was taken in April 2013 using the Wide Field Camera (WFC) mounted on the 2.5m *INT* telescope at the Observatorio del Roque de los Muchachos (ORM), La Palma. The WFC is an optical mosaic camera consisting of 4 CCDs of 2098 × 4100 pixels (0.33 arcsec/pixel). Mrk273 was always observed with CCD4, which has the highest efficiency at red wavelengths. For these observations we used the Filter#228 ($\lambda_c$ = 6813Å, FWHM =

| Slit Position | Slit PA degrees | Exp time (s) | Airmass | Seeing (arcsec) |
|---|---|---|---|---|
| Pos1 | 70 | 6000 | 1.24 | 0.9-1.1 |
| Pos2 | 56 | 7200 | 1.14 | 0.9-1.2 |
| Pos3$^\star$ | 70 | 7200 | 1.24 | 0.9-1.2 |
| Pos4$^\star$ | 56 | 6000 | 1.14 | 0.9-1.1 |

Table 2 Log of the *INT* IDS spectroscopic observations of Mrk273 (z = 0.0373) used for this paper. The seeing (FWHM) was estimated using field stars in the acquisition images.
$^\star$ These two slits (Pos3 and Pos4) were placed at exactly the same PA as Pos1 and Pos2 respectively, but were shifted by 1 arcsec to the North. For clarity, the slit positions 3 and 4 are not shown in Figure 3.

93Å), which is centered on the H$\alpha$ emission line[2] and includes the [NII]$\lambda\lambda$6549,6583 doublet. In order to remove the cosmic rays, hot pixels and other artifacts we took four 700s exposures dithered on four positions in the sky. Unfortunately, due to some technical difficulties during the night of the observations we could not acquire a line-free continuum image in a wavelength range adjacent to H$\alpha$. Therefore, no continuum subtraction could be performed in the case of the *INT*-WFC image of Mrk273 presented in this paper. The seeing during the observations, measured with foreground stars in the images, was FWHM = 1.5 – 1.6 arcsec. Details of the INT/WFC observations are shown in Table 1

We used a series of IRAF routines to perform the standard reduction process, including bias subtraction, flat-field correction and cosmic ray rejection. Any remaining cosmic rays after the initial reduction were cleaned "manually" using the routines IMEDIT in IRAF and/or CLEAN within the STARLINK package FIGARO. To transform into physical units we used two standard stars observed with the exact same set-up used for the observations of the galaxy, and calculate a factor to transform counts s$^{-1}$ into ergs s$^{-1}$ cm$^{-2}$. The calibration factor obtained for each of the stars is identical and the estimated flux calibration uncertainty is 7%. The flux calibrated INT image is shown in Figure 2.

Finally, we have followed the same procedure described in the previous section for the *HST* images and compared the flux calibration of the *INT*-WFC image with that of the existing *WHT*-ISIS spectroscopic observations of the galaxy (Rodríguez Zaurín et al. 2009). If we define $F_{WFC}$ as the integrated flux over the spatial extent of the galaxy covered by the slit in the WFC image, we find that $F_{WFC}/F_{WHT}$ = 0.8, i.e. the flux calibrations for the two observations are in good agreement.

### 2.2. Spectroscopic data

Long-slit optical spectroscopic observations were taken for Mrk273 in May 2013 using the Intermediate Dispersion Spectrograph (IDS) on the *INT* . The observations were obtained using the R400V grating centered at 5250Å with the RED+2 CCD. The instrumental set-up resulted in a spatial scale of 0.44 arcsec pix$^{-1}$, and a dispersion of 1.5 Å pix$^{-1}$. The useful wavelength range is $\sim$ 4000 – 7200 Å. The data were reduced (bias subtracted, flat field corrected, cleaned

[2] We assume a systemic redshift of $z = 0.0373$ for the system (see RV13). All the radial velocity shifts presented in this paper are measured relative to this redshift.

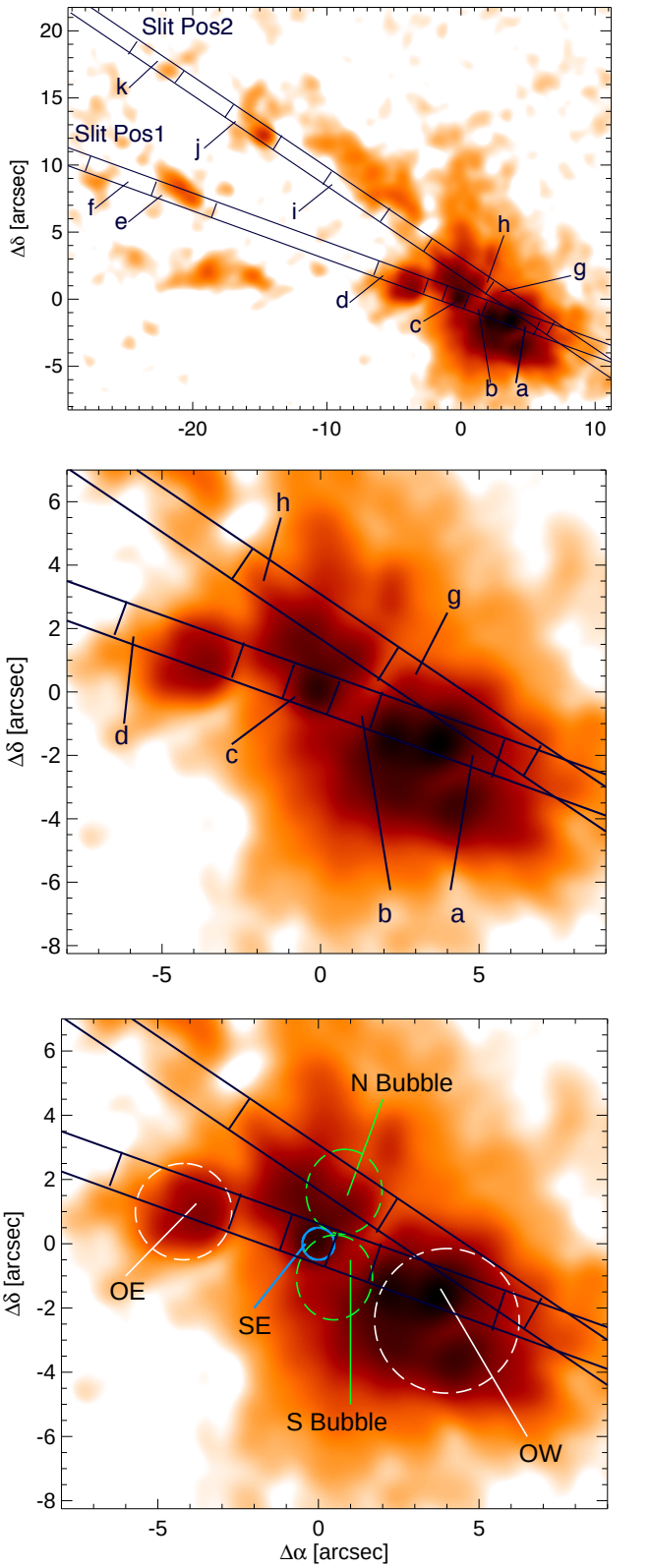


Fig. 3 Upper panel: *HST* continuum subtracted [OIII] image of the galaxy showing the location of the slits and the extraction apertures. The images have been convolved with a Gaussian of FWHM = 1" to simulate the seeing conditions during the spectroscopic observations. Medium and lower panels: these two figures are a zoom into the nuclear region of the galaxy. The figures show in detail the main regions of interest that will be later analyzed in the paper (see the text for details) and the apertures that cover those regions. (A color version of this Figure is available in the online journal).

of cosmic rays, wavelength calibrated and flux calibrated) and straightened before extraction of the individual spectra using the standard packages in IRAF and the STARLINK packages FIGARO and DIPSO. The wavelength calibration accuracy, as determined using the mean shift between the measured and published (Osterbrock et al. 1996) wavelength of night-sky emission lines, is ∼0.35 Å (20 km s$^{-1}$). The spectral resolution, calculated using the widths of the night-sky emission lines (FWHM), is 3.1±0.1Å at 6300 Å(∼145±5 km s$^{-1}$). The estimated uncertainty for the relative flux calibration is ±5%, based on comparison of the response curves of various spectrophotometric standard stars observed during the observing runs. Finally, the seeing during the observations, measured using stars in the acquisition image, was 0.9 – 1.2 arcsec. Details of the *INT* IDS observations for Mrk273 can be found in Table 2.

For these observations we used 4 slit positions selected to include the main ionized gas features observed in our ACS-[OIII] image of the galaxy. Two slits were placed at PA 70, plus another two at PA 56. The relative shift between each pair of slits at the same PAs was 1 arcsec to the north. The slits cover the bright [OIII] emission in the nuclear region of the galaxy as well as a significant fraction of the faint, very extended [OIII] emission observed towards the east of the nuclear region.

The extraction apertures for each slit position were selected based on spatial cuts of the 2D-frames in wavelength ranges chosen to include the [OIII]λ5007 and the Hα+[NII] emission lines. The slit position and the corresponding extraction apertures for Pos 1 and 2 are shown in Figure 3, overplotted onto the continuum subtracted [OIII] image of the galaxy. To simulate the seeing conditions during the spectroscopic observations, the [OIII] image in the figure has been convolved with a Gaussian of FWHM = 1 arcsec.

Since we aim to compare our results with those of previous studies of the galaxy, it is crucial to know the precise location of the slits. To that aim, we followed again the same procedure as described in section 2.1.1 to find the location of the slits on the *HST* images with a precision of 5 pixels (0.25 acsec). In addition, we checked the consistency of the flux calibrations for the entire dataset used in this paper by comparing the *INT*-IDS observations with the *HST* images. If we define $F_{IDS}$ as the integrated flux over a espatial slice extracted from the spectra using wavelength ranges selected to match those of the *HST* filters, we find that $F_{HST}/F_{IDS}$ is equal to 0.87 and 0.78 for the continuum and [OIII] observations respectively. Overall, the flux calibrations for the different datasets used for this paper show a high degree of consistency.

## 3. Results

### 3.1. Imaging

#### 3.1.1. *HST* imaging: the detailed morphology of the ionized gas emission

The most remarkable feature visible in our emission-line-free, F550M continuum image of the galaxy (upper-left panel in Figure 1) is the well known extended tail to the south of the galaxy. Note that the F550M continuum image of the galaxy does not cover the full extent of the tail (∼36 kpc or ∼46". See for example, Kim et al. 2002, their Figure 1). The image also shows some weak, but significant continuum emission towards the north-east of the nuclear region and to the west of the tidal tail. The lower-left panel in our Figure 1 shows the morphology of the continuum emission in the central 15×15 arcsec. There is a large number of bright knots, clumps and other irregular condensations around the brightest "L-shaped" structure close to the N and SE nuclear components. All of these structures are crossed by dust features, with the most prominent dust lane observed to the east of the nuclear region, extended from north to south, and then along the tidal tail.

Figure 1 shows the continuum subtracted [OIII] image of the galaxy. This is strikingly different from the continuum image. The first notable structure in the image is the spectacular system of extended filaments and clumps to the east of the galaxy. Such clumps and filaments extend ∼25" (∼19 kpc) in our [OIII] image; the average position angle of the structure, as measured relative to the N nucleus, is ∼68°, and the range of position angles covered by the structure ∼50°.

To better study the morphology of the [OIII] emission in the nuclear region, the lower-right panel in Figure 1 concentrates on the [OIII] emission from the central 15×15 arcsec of the galaxy. The locations of the N, SW and SE components are indicated in the figure with open circles. It is notable that the [OIII] emission is not particularly enhanced at the location of the N and SW nuclei, likely related to reddening effects. However, coinciding with the location of the SE component we find the brightest and most compact condensation of [OIII] emission observed in our images. To estimate the size of this feature we fitted a 2D Gaussian to the region. The resulting FWHM ($FWHM_{unc}$) was corrected for instrumental width ($I_{FWHM}$) by subtracting the two values in quadrature[3]. The corrected FWHM is $FWHM_{corr}$ = 0.13±0.02 arcsec (99±15 pc). Therefore, although the SE component is compact, it is resolved in our observations.

The lower-right panel in Figure 1 also shows a schematic of the nuclear-superbubble model proposed by RV13 in their recent IFS study of the galaxy. Interestingly, the figure shows a "U-shaped" structure of diffuse [OIII] emission that closely follows the structure of the northern, near side of the bipolar superbubble (referred here as "N-Bubble"). However, the southern, far side of the bubble ("S-Bubble") is not clearly visible in our image, which is likely related to reddening effects. Finally, on larger scales, but still within the central ∼15 arcsec, there are two high surface brightness structures of enhanced [OIII] emission extended ∼5 arcsec (4 kpc) to the east and west of the nuclear region, almost perpendicular (PA∼80°) to the RV13 nuclear supperbubble. "Overall, the structure of the [OIII] emission in the nuclear regions is highly complex. A detailed spectroscopic study of the different structures described in this section is carried out later in the paper.

[3] The instrumental width ($I_{FWHM}$) was measured using the same 2D Gaussian fit for two stars in the field. We obtained $I_{FWHM}$ = 0.115±0.005 arcsec. The FWHM of the SE component before the correction is $FWHM_{unc}$ = 0.174±0.005 arcsec. The corrected FWHM is calculated as $FWHM_{corr} = \sqrt{FWHM^2_{unc} - I^2_{FWHM}}$.

#### 3.1.2. *INT* imaging: low surface brightness emission at large scales

The *HST* images of Mrk273 show no evidence for [OIII] emission at or around the tidal tail to the south of the galaxy. There are two possible explanations for this finding. The most straightforward explanation is that there is no ionized gas at these locations. This would be consistent with the results of Rodríguez Zaurín et al. (2009), from their detailed study of the stellar populations in the galaxy. These authors found that the optical (3000 – 7500Å) continuum of the source along the tidal tail is remarkably uniform, and is adequately modeled using a stellar population of age ∼700 Myr that dominates the optical emission, with a small contribution from a young (i.e. ionizing) stellar population.

However, given the size of the resolution element of the ACS-WFC, it is possible that some low-surface-brightness emission line features are not detected in our *HST* images. In order to detect such faint features with the ACS camera, one would require substantially longer exposure times than those used for our observations. An alternative is to use deep, lower resolution images. In this context, Figure 2 shows our deep, H$\alpha$+[NII] image of the galaxy taken with the Wide Field Camera (WFC) at the *INT* telescope. The seeing during these observations was ∼1.6". Therefore, none of the detailed nuclear structure visible in the *HST* images is distinguishable in Figure 2. However, the figure shows extended, diffuse emission to the east of the galaxy extended ∼30 arcsec (∼23 kpc) from the nuclear region and to the west of the southern tail.

Unfortunately we do not have a deep INT/WFC line-free continuum images to allow accurate quantification of the continuum contribution to the extended structures visible in the INT narrow-band image. However, we note that the filamentary structure to the west of the southern tidal tail has a peak surface brightness that is ∼50% of the that of the tidal tail itself. If this were predominantly a continuum structure, we would expect it to be visible at a similar contrast level in our F550M continuum image and HST broad-band images of the source that are continuum-dominated (e.g. the *HST* F435W and F814W images presented in Mazzarella & Boroson 1993; Hibbard & Yun 1996; Kim et al. 2002). The fact that the diffuse emission to the west of the southern tidal tail is in fact much fainter in the latter images, provides strong evidence that the western filaments – that run parallel to the main tidal tail – are predominantly emission line structures.

We further note that the western filamentary structure partially follows the morphology of the extended X-ray nebula reported by Iwasawa et al. (2011). Their results, based on new *Chandra* X-ray observations of the source, are consistent with the tidal tail being located in front of the soft X-ray nebulae in our line of sight, such that the soft X-ray emission is partially absorbed by the cold gas in the tidal tail. Moreover, Iwasawa et al. (2011) derived a lower limit on the column density of $N_{\rm H} \sim 10^{22}{\rm cm}^{-2}$, similar to that of edge-on galaxy disks, and consistent with other measurements of disk shadowing (Barber et al. 1996). Iwasawa et al. (2011) concluded that the source of the soft X-ray emission is likely to be star formation in the edge-on disk, which would be, a priori, consistent with our *INT*-WFC image. In this scenario, the highly reddened, young stellar populations in the disk would not make a large contribution to the visible optical emission at these locations, which would explain the Rodríguez Zaurín et al. (2009) results for the stellar populations along the tail. Note however, that while Iwasawa et al. (2011) found soft X-ray emission on both sides of the tidal tail, H$\alpha$+[NII] emission is only detected to the west of the tail in our *INT*-WFC image. Future, deeper H$\alpha$ images of the galaxy will help to investigate in detail the extended ionized gas emission around the tail and its relation with the soft X-ray emission at these locations.

| Extraction Aperture (AP) (1) | kin Comp (2) | FWHM km s$^{-1}$ (3) | $\Delta V$ km s$^{-1}$ (4) | H$\beta$ erg s$^{-1}$ cm$^{-2}$ (5) | [OIII]$\lambda$5007 (6) | [OI]$\lambda$6300 (7) | H$\alpha$ (8) | [NII]$\lambda$6583 (9) | [SII]$\lambda$6716,6731 (10) |
|---|---|---|---|---|---|---|---|---|---|
| IDS-POS1 | | | | | | | | | |
| a$^{\star}$ | N1 | 158±26 | -64±22 | 8.36E-16 | 13.53 | 0.56 | 4.17 | 5.71 | 2.11 |
| | N2 | 482±31 | -41±22 | 5.01E-15 | 6.41 | 0.36 | 2.99 | 2.74 | 1.52 |
| | B | 1458±157 | -204±79 | 0.33 | 1.92 | 0.24 | 2.295E-15 | 3.01 | 1.18 |
| b | N | 212±30 | -12±25 | 2.99E-16 | 11.68 | 1.06 | 7.73 | 7.32 | 4.34 |
| | I1 | 644±28 | -173±32 | 1.20E-15 | 9.00 | 0.76 | 7.02 | 6.54 | 3.74 |
| | I2 | 623±64 | 411±46 | 2.08E-16 | 4.36 | 1.40 | 5.02 | 15.07 | 2.67 |
| c | N | 431±33 | -16±21 | 2.12E-15 | 3.52 | 0.79 | 3.93 | 2.77 | 2.64 |
| | B | 1407±59 | 111±33 | 5.66E-16 | 5.34 | 1.94 | 6.44 | 19.32 | 5.72 |
| d | N1 | 193±46 | 285±25 | 2.87E-16 | 2.11 | ... | 5.35 | 4.31 | 1.64 |
| | N2 | 362±53 | 95±43 | 6.84E-16 | 7.35 | 0.15 | 3.15 | 1.41 | 0.89 |
| | I | 876±122 | 73±48 | 3.70E-16 | 8.20 | 1.69 | 4.09 | 8.48 | 6.34 |
| e | N | 63±21 | 67±24 | 3.43E-16 | 7.27 | ... | 1.67 | 0.65 | ... |
| f$^{\dagger}$ | N | 38±15 | 114±27 | ... | 9.94E-16 | ... | ... | ... | |
| IDS-POS2 | | | | | | | | | |
| g | N1 | 163±22 | -13±23 | 9.46E-16 | 9.47 | 0.89 | 5.24 | 6.23 | 2.93 |
| | N2 | 392±43 | -166±30 | 1.78E-15 | 5.75 | 0.31 | 4.80 | 3.25 | 2.26 |
| | I | 856±63 | -73±34 | 9.53E-16 | 12.57 | 1.27 | 8.36 | 16.75 | 7.87 |
| h$^{\star}$ | N | 149±23 | -22±23 | 1.26E-15 | 0.56 | 0.26 | 6.44 | 1.98 | 1.60 |
| | I | 500±26 | 94±23 | 5.35E-15 | 2.70 | 0.87 | 6.96 | 8.00 | 4.48 |
| | B | 1518±116 | -468±10 | 0.33 | 0.54 | 0.2 | 8.57E-15 | 1.85 | 0.67 |
| i | N | 111±25 | -77±24 | 2.23E-16 | 8.97 | ... | 3.33 | 2.26 | ... |
| j | N | 84±32 | -26±23 | 3.18E-16 | 12.14 | ... | 4.10 | 2.05 | ... |
| k$^{\dagger}$ | N | 95±29 | 43 ±27 | ... | 1.106E-15 | ... | ... | ... | ... |

Table 3 The modeling results for the different kinematic components within the extraction apertures. Col (1): aperture label as indicated in Figure 3. Col (2): The label of the different components as defined in Section 3.2.1: N (narrow), I (intermediate) and B (broad). For those apertures with two components within the same FWHM range, these are indicated with numbers (e.g. N1 and N2 corresponding to the two narrow components detected in Ap-a). Col (3) and (4): Instrumentally-corrected line widths (FWHM) and shifts ($\Delta V$) measure relative to galaxy rest frame (defined as z = 0.0373, RV13). The uncertainties in these values were estimated accounting for the uncertainties from the modeling and the systematic calibration errors (i.e. the uncertainty in the instrumental width and the wavelength calibration error). Column (3): H$\beta$ flux in erg s$^{-1}$ cm$^{-1}$. From Columns (4)–(10): ratios of the fluxes of the main emission lines to the H$\beta$ line. The uncertainties in these ratios are typically $\lesssim$15 per cent, as estimated accounting for the 5 per cent flux calibration uncertainty, and the uncertainties in the model fits themselves. However, there are a some particular cases, mainly those kinematic components that make a small contribution to the flux, for which the uncertainty can be as high as 50 per cent (for example, the B component of the AP-a). These line ratios are not corrected for reddening.

$^{\star}$ For these two apertures the contribution of the broad component (B) to the overall H$\beta$ flux is negligible. Therefore, when such component is included in the modeling its properties are entirely unconstrained, leading to unrealistic line ratio values. For the broad component in these two apertures, the fluxes are given relative to the H$\alpha$ line. In addition, when calculating the line ratios used later for the diagnostic line ratio diagrams we took the conservative approach of assuming an H$\alpha$ to H$\beta$ ratio of 3. Note that, since reddening effects are expected to be important at the locations in the galaxy covered by these extraction apertures (i.e. the H$\beta$ flux will be in reality less than 3 times the H$\alpha$ flux), the [OIII]/H$\beta$ line ratios calculated are lower limits of the real values.

$^{\dagger}$ For these two extraction apertures, only the [OIII]$\lambda\lambda$4959,5007 emission lines are detected. The table show the [OIII]$\lambda$5007 flux in units of erg s$^{-1}$ cm$^{-1}$.

### 3.2. Spectroscopy

#### 3.2.1. Continuum emission subtraction

Prior to the modeling of the emission line profiles in the nuclear regions, the spectra were shifted to the galaxy rest frame ($z = 0.0373$: RV13). Since we aim to study not only the kinematics but also the ionization mechanisms in Mrk273, it is important to subtract the underlying stellar continuum prior to modeling the emission line profiles. This might be an important issue for the H$\beta$ and H$\alpha$ emission lines, which are are the most affected by the stellar absorption. Unfortunately, our *INT*-IDS spectra do not have sufficient wavelength range coverage to carry out a detailed analysis of the stellar populations. For this reason, we used the results of spectral synthesis model fits to the wider-coverage (3000–7500Å) *WHT*-ISIS spectra of this source, as presented in Rodríguez Zaurín et al. (2009), to guide our fits to the stellar continuum of the INT/IDS data.

Rodríguez Zaurín et al. (2009) found that the stellar populations across the full extension of the galaxy covered by their slit (see Figure 3) were remarkably uniform in terms of their ages, with no evidence for a significant age gradient. The best fitting models in the central regions (their apertures D, E and F) comprise a ∼0.7–1.0 Gyr ($E(B-V) \leq 0.4$) stellar population plus a significant contribution from a reddened $\lesssim$50 Myr ($E(B-V) \leq 1.0$) stellar population (see Rodríguez Zaurín et al. (2009) for details). Therefore, we took the approach of assuming a similar mix of stellar populations to correct for the stellar continuum the *INT*-IDS spectra. This approach was used only for those apertures that sample regions with significant continuum emission, as observed in the ACS continuum image of the source. These are: AP-a, b, c, d, g and h.

The stellar population within the apertures with significant stellar continuum were modeled using a similar technique to that described in Rodríguez Zaurín et al. (2009), but using a smaller number of discrete values for the age and reddening of the stellar populations (see Rodríguez Zaurín et al. (2009) for details). Although it is beyond the scope of this paper to perform a detailed analysis of the stellar populations in the galaxy, we emphasize that models including a 0.7 Gyr ($E(B-V) = 0.2$) plus a <10 Myr ($0.5 < E(B-V) \leq 1.0$) stellar population of varying contribution (25–90%), accurately reproduce the stellar continumm emission from the galaxy for these 6 apertures.

Overall, we find that subtracting the stellar continuum is important to better constrain the properties of the different kinematic components, especially for the H$\beta$ emission line. For example, 3 kinematic components are required to adequately model the H$\alpha$ or the [OIII]$\lambda\lambda$4959,5007 emission lines at almost all locations in the nuclear regions. However, before subtracting the stellar continuum, there are cases where only two of these components are required when modeling H$\beta$. In these cases we often find that the third kinematic component, typically the one that makes the smallest contribution to the overall H$\alpha$ emission, clearly emerges once the stellar emission has been subtracted from the spectra. The change in flux for the kinematic components detected before subtracting the stellar continuum is small for H$\beta$, a factor of $\lesssim$1.3. In the case of the H$\alpha$ emission line, the effects of correcting from stellar absorption are negligible.

#### 3.2.2. Fitting the emission line profiles

Following continuum subtraction, we used a combination of *DIPSO* and the IDL MPFIT (Markwardt 2009) code to fit Gaussian profiles to the emission lines. Our modeling approach is described in detail in Rodríguez Zaurín et al. (2013). To summarize, we first selected a prominent emission line that is sufficiently bright and unblended to allow the generation of a model that could be used to fit all the other emission lines. In this context the strong [OIII]$\lambda\lambda$4959,5007 lines usually have high S/N in our spectra, are in a region clean from any atmospheric absorption, and are not blended with other emission lines. We fit these emission lines with the minimum number of Gaussian components required to produce an acceptable fit. The number of Gaussian components required in the model for each line was determined using both an assessment of the reduced Chi squared ($\chi^2{}_{red}$) values and visual inspection of fits overlaid on the data. For example, models comprising two kinematic components resulted in $\chi^2{}_{red}$ values of 2.4-4 for Ap-a, b, d and h (See Fig 3 and 4 ). Including a third, more kinematically disturbed, component resulted in a significant decrease in the $\chi^2{}_{red}$, down to values of one or less. A similar reduction in $\chi^2{}_{red}$ was not seen when we added a second or third kinematic component in the cases of the SE compact structure (Ap-c), and in regions covering the extended arc structures to the east (e.g. Ap-j).

In addition, when fitting the [OIII] lines we used three constraints in accordance with atomic physics: i) the flux ratio between [OIII]$\lambda$5007 and [OIII]$\lambda$4959 was set at 2.99:1 (based on the transition probabilities); ii) the widths of the corresponding kinematic components of each line were forced to be equal; iii) the shifts between the corresponding components of each line were fixed to be 48.0Å. We will refer to the model fitted to the [OIII] lines in this way as the "[OIII] model" in what follows.

Once the [OIII] model has been derived, we attempted to model the other prominent emission lines in the spectra with the same kinematic model (velocity widths and shifts) as [OIII], leaving the relative fluxes in the kinematic subcomponents to vary. As well as the constraints derived from the [OIII] model, we further constrained the fits to other doublets in accordance with atomic physics (see RZ13 for details). After a series of iterations, the initial [OIII] model was refined so that the final kinematic model is the best fitting model that adequately reproduces all the prominent emission lines in the spectra. The velocity widths derived from the fits were quadratically corrected for the instrumental profile, and all linewidths and radial velocity shifts were corrected to the rest frame of the object (z = 0.0373).

Table 3 shows the velocity shifts, widths, line fluxes and emission line rations, for slit positions Pos1 and Pos2. Note that the line ratios in the table have not been corrected for reddening. This is because estimating the reddening is challenging based just on our existing data. H$\alpha$ is in a blend, and there are potentially degeneracies involved in the fits that may affect the accuracy of the line ratio measurements, particularly in the case of the highly complex emission line kinematics present in the near-nuclear regions of Mrk273.

As mentioned in Section 2.2, two additional long-slit spectra were taken at the exact same PAs as Pos1 and Pos2 but shifted one arcsec to the North. These are referred as Pos3 and Pos4 in Table 2 . For each of these two additional slit positions we extracted a set of 4 extraction apertures

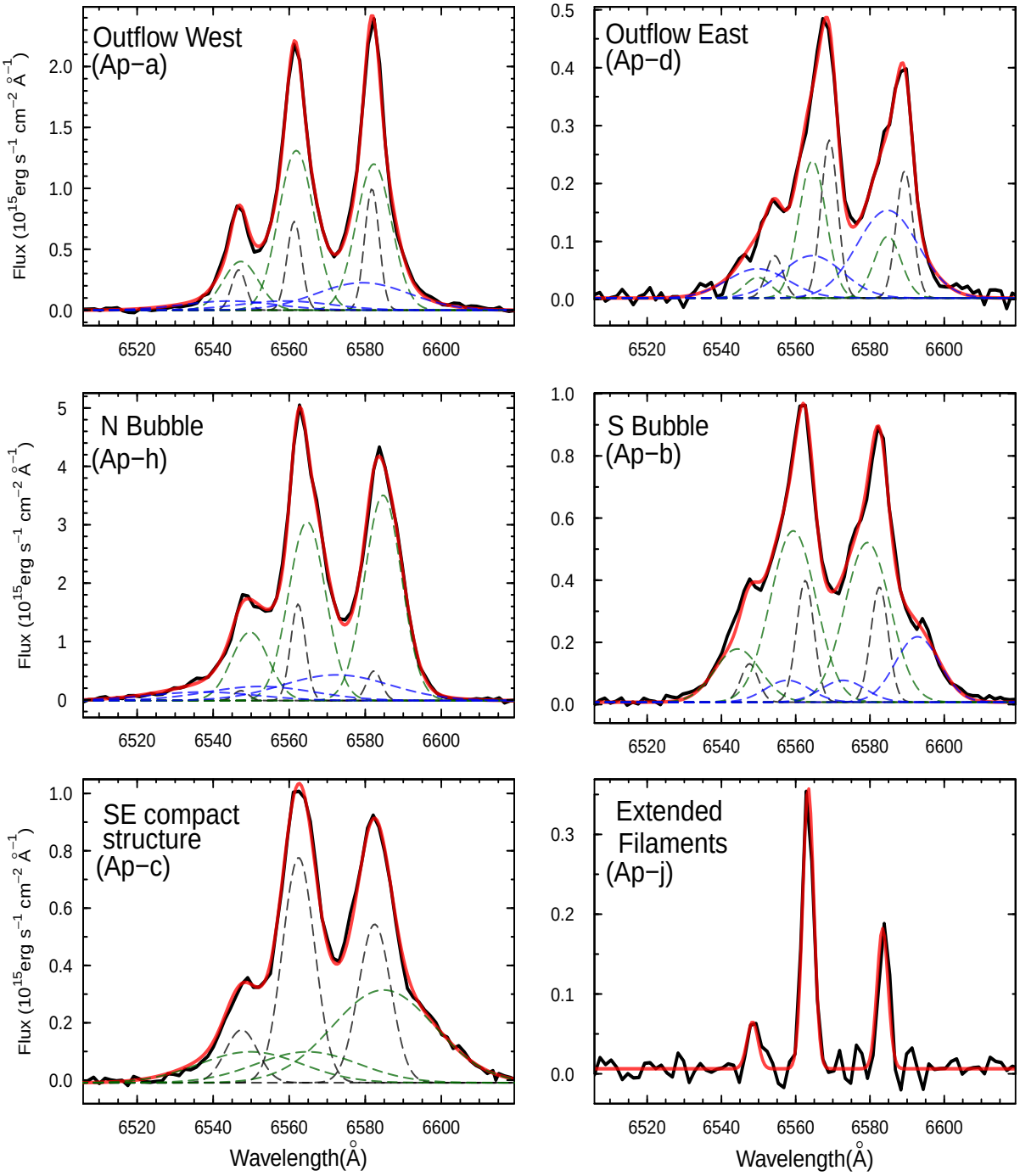


Fig. 4 The emission line modeling results for the H$\alpha$ ($\lambda_{\rm rest}$ = 6563Å) and the [NII] emission lines ($\lambda_{\rm rest}$ = 6548 and 6583Å). The black solid line represents the data, while the red solid line represents the overall fit to the emission lines. Black, green and blue dashed lines correspond to the different kinematic components in order of increasing FWHM. The region of the galaxy corresponding to each of the emission line profiles, and the extraction aperture that samples that region, are also indicated in the figure. (A color version of this Figure is available in the online journal.)

respectively that sample similar regions to those sampled by Pos1 and Pos2 (but 1 arcsec immediately to the north). The modeling results are, in general, consistent with those for Pos1 and Pos2 and therefore are not shown in Table 3.

In order to compare with the recent RV13 optical IFS study, which involves fits to the H$\alpha$+[NII] complex, Figure 4 shows the fits to the H$\alpha$+[NII] emission lines profile for 6 extraction apertures selected to sample the main regions of interest, as observed in our *HST* images. These are: Ap-a, Ap-b, Ap-c, Ap-d, Ap-h and Ap-j (see Figure 3 for their location in the galaxy). In Figure 4, the apertures are also labelled according to the region that they cover. Ap-a and Ap-d sample the outflowing gas to the west and east of the nuclear region, and therefore are labelled as "Outflow-West" and "Outflow-East" respectively. Ap-b and Ap-h sample the lobes of the nuclear superbubble found by RV13 to the south and north of the nuclear region and are labelled as "N-Bubble" and "S-Bubble" respectively. Finally, Ap-c

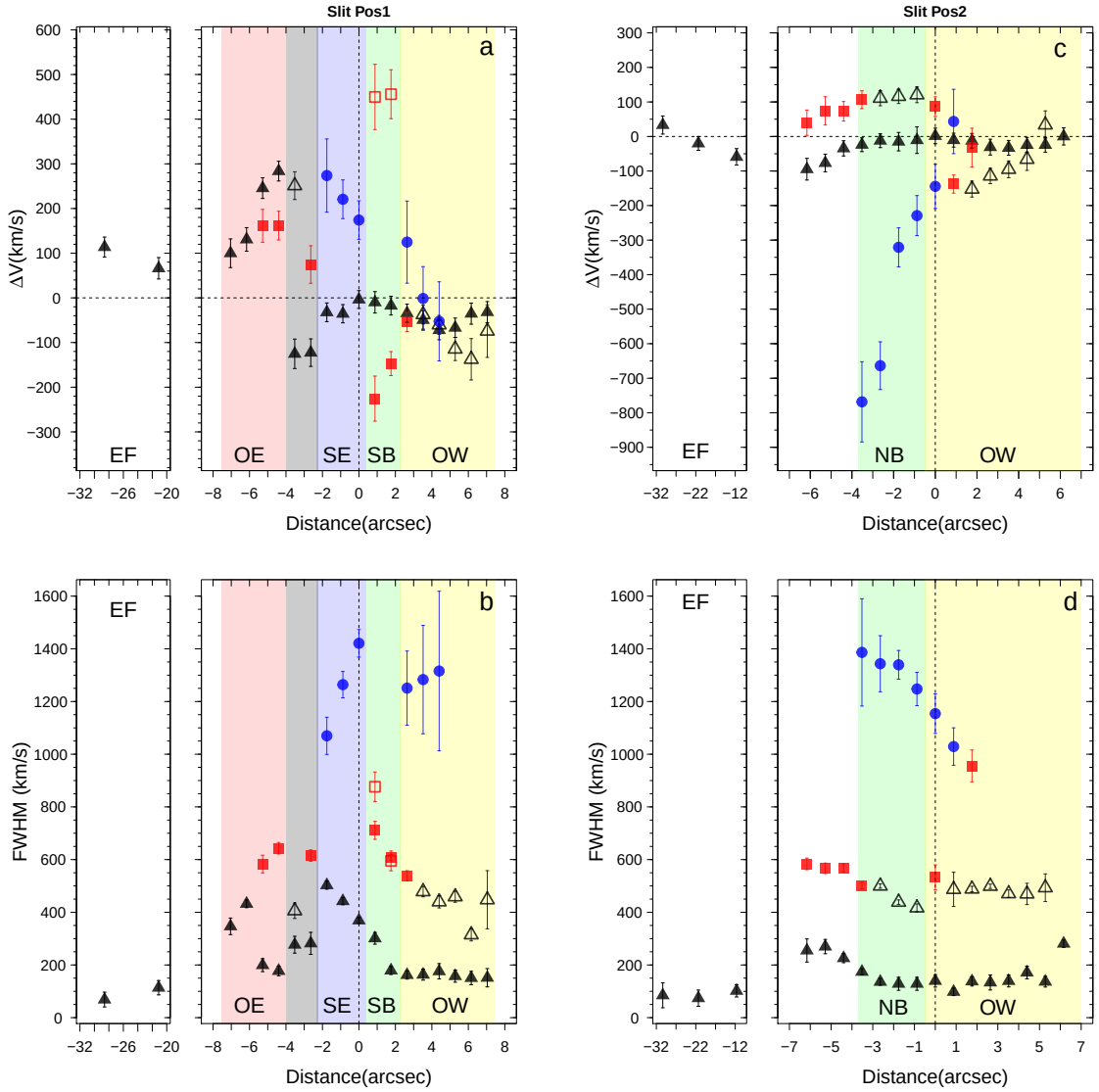


Fig. 5 Velocity shifts (ΔV) and widths (FWHM, corrected for instrumental width) plotted against the distance from a reference point in the galaxy, for Slit Pos1 and Pos2 (see the text for details on the selection D = 0 arcsec reference point). Extraction apertures of 2 pixels (i.e 0.88 arcsec) were used for the Figure, except at the very extended regions, where we used the apertures Ap-e and Ap-f for Pos1 and Ap-i, Ap-j and Ap-k for Pos2. Black triangles, red squares and blue circles correspond to the narrow, intermediate and broad components. To help the reader associate the points in the upper panels to those in the lower panels, when more than one kinematic component within the same FWHM range is present at a certain location, the second or third component (typically the broader) is indicated with an open symbol. For example, in Figures 5a and 5b, the ionized gas emission at D∼7 arcsec is modeled using two kinematic components of widths FWHM = 152±25 and FWHM = 456±106, i.e. both within the narrow FWHM range. To be able to unambiguously associate the points in Figure 5a to those in Figure 5b at this location, the broader component is plotted with an open triangle. Finally, the shaded regions indicates the location in the galaxy. For Pos1, from west to east: yellow, green, blue and red correspond to Outflow-West (OW), S-Bubble (SB), SE compact structure and Outflow-East (OE) respectively. In addition, the grey-shaded region corresponds to the prominent dust lane observed to the east of the nuclear region. For Pos2, yellow and green correspond to Outflow-West and N-Bubble (NB) respectively. The region corresponding to the extended filaments (EF) is also indicated in the Figure. A color version of this Figure is available in the online journal.

and Ap-j sample the compact SE structure in the nuclear region and the filaments of clumps of extended emission, and are labelled as "SE compact structure" and "extended filaments". See Figures 3 and 4 for details.

For ease of reference in the following sections, we use the following scheme to label kinematic components, based on line widths (FWHM):

– narrow: FWHM $< 500$ km s$^{-1}$ ;

– intermediate: $500 \leq$ FWHM $< 1000$ km s$^{-1}$ ;

– broad: FWHM $\geq 1000$ km s$^{-1}$ .

## 4. Discussion

### 4.1. Ionized gas Kinematics

Although the spatial resolution of the long-slit observations is not as good as that of the HST images, they are useful to gain a general idea of the ionized gas kinematics at different locations in the galaxy. In this context, Figure 5 shows the velocity shifts ($\Delta$V) and widths (FWHM) along the slits Pos1 and Pos2. For this figure, we have used extraction apertures of 2 pixels (i.e 0.88 arcsec) except at the very extended regions, where we used the apertures Ap-e and Ap-f for Pos1 and Ap-i, Ap-j and Ap-k for Pos2. Since the kinematics of the galaxy are highly disturbed across the slits, the selection of a reference point (D = 0 arcsec) is rather arbitrary. In the case of Pos1, the reference point is the centroid of the SE structure (i.e. RA=0 and Dec=0 in Figures 1 and 3), while for Pos2, the reference point coincides with the boundary region between Ap-g and Ap-h in Figure 3.

Figure 5 shows that the kinematics in Mrk273 are disturbed at almost all locations in nuclear regions of the galaxies. For example, the narrow and intermediate components across Pos2 are well organized around the reference point (D=0 arcsec). However, a third kinematic component emerges as we approach that point, and extends into the so called N-Bubble region. Consistent with the results of RV13, we find extreme velocity shifts and widths of up to $\Delta$V$\sim$-1000 km s$^{-1}$ and FWHM$\sim$1400 km s$^{-1}$ respectively, at these locations. In contrast, the emission line profiles along slit Pos1 change drastically from one region to another. The kinematic properties of the narrowest component (black-filled triangles) are relatively uniform across the region of $\sim$10 arcsec that expands from Outflow-West to the prominent dust lane[4]. However, across this region, 1 or 2 additional kinematic components with substantially different widths and shifts are required to adequately model the emission line profiles.

Finally, Figure 5 also show the velocity shifts and widths of the ionized gas in the so-called extended filaments (Ap-e, Ap-f, Ap-i, Ap-j and Ap-k in Figure 3). Interestingly, the emission lines at these locations show small velocity shifts and have the narrowest FWHM values (38–111 km s$^{-1}$). In addition, the figure shows the presence of a positive velocity gradient across the filaments. This is further confirmed using the results from slit Pos3 and Pos4, which sample a larger fraction of the emission from the filaments observed in our ACS images.

Overall, Figure 5 illustrates the complexity of the gas kinematics in Mrk273.

### 4.2. Ionization Mechanisms

#### 4.2.1. AGN and starburst photoionization

In this section we investigate the nature of the ionizing source(s) responsible for the emission lines observed at the different locations in Mrk273. Figure 6 shows the diagnostic line ratio diagrams (Baldwin et al. 1981; Veilleux & Osterbrock 1987, hereafter BPT/VO87 diagrams) along with the optical classification scheme of Kewley et al. (2006). Overplotted on the figure are the results from our kinematic study. For this figure we have used the extraction apertures shown in Table 3 plus the 8 apertures extracted for Slit Pos3 and Pos4. In addition we also used the Rodríguez Zaurín et al. (2009) *WHT*-ISIS spectrum of the source and modeled the emission lines for their nuclear extraction apertures (apertures D, E and F in their paper). Overall, a total of 22 apertures, that sample almost the entire nuclear emission, and a large fraction of the emission at larger scales, were used to generate the plots in Figure 6. The black triangles, red squares and blue circles correspond to the narrow, intermediate and broad components respectively. For clarity, no individual error bars are shown in the Figure. However, to give an idea of the uncertainty associated to the line ratio measurements a "cross symbol" indicates the median of all line ratio errors in each respective diagram. Individual error bars are shown later in the section, when a detailed analysis of some regions of interest is performed.

In the first place, it is notable that the line ratios measured at almost all locations in the galaxy are consistent with a Sy2 classification, although a significant fraction of the points in Figure 6 falls close to the Sy2/LINER limiting region. We find that the intermediate and broad components tend to have higher [NII]/H$\alpha$, [OI]/H$\alpha$ and [SII]/H$\alpha$ line ratios than the narrow components. Interestingly, such trend is not observed for the [OIII]/H$\beta$.

With the aim of better understanding the nature of ionization mechanisms responsible for the measured line ratios, Figure 6 also shows the Groves et al. (2004) dusty, radiation pressure-dominated photoionization models for NLR in AGN. For these models we assume a hydrogen density $n_H$ = 1000 cm$^{-3}$ and 4 times solar abundance (4Z$_\odot$). This latter value was chosen based on the recent results of RZ13. These authors found that the line ratios derived for the ULIRGs in their sample were consistent with gas of super-solar abundances (4Z$_\odot$) photoionized primarily by an AGN. A grid of models for various values of the ionizing parameter ($U_0$ = 0, -1, -2, -3, -4) and ionizing continuum SED power-law indicies ($F_\nu \propto \nu^\alpha$, $\alpha$ = -1.2, -1.4, -1.7, -2.0) is shown in the figure.

In general, AGN photoionization models reproduce the emission line ratios well, in the sense that there is good consistency in the relative positions of the points and the models between the different diagrams. Interestingly, the biggest disagreement between the models and the observed line rations occurs for the narrow kinematic components, for which the degeneracy issues mentioned in Section 3.2 are least important (i.e. the flux associated with these components is better constrained). Finally, We have explored models with lower metallicities (Z$_\odot$ and 2Z$_\odot$), and higher and lower densities (100 and 10000 cm$^{-3}$), and the level of agreement not only does not improve, but it is worse.

#### 4.2.2. Shock Ionization

As well as photoionization by AGN and starburst, it is possible that line ratios plotted in Figure 6 might be explained in terms of ionization by fast radiative shocks (Dopita & Sutherland 1995, 1996; Groves et al. 2004; Allen et al. 2008). Indeed shocks are a plausible mechanism for accelerating the gas to the velocities we measure in the nuclear regions of Mrk273. The shock models predict a series of line ratios for a range of magnetic field strengths ($B$), electron

[4] Given the significant reddening effects, the kinematic results within the dust lane (i.e. the grey-shaded area) should be interpreted with caution.

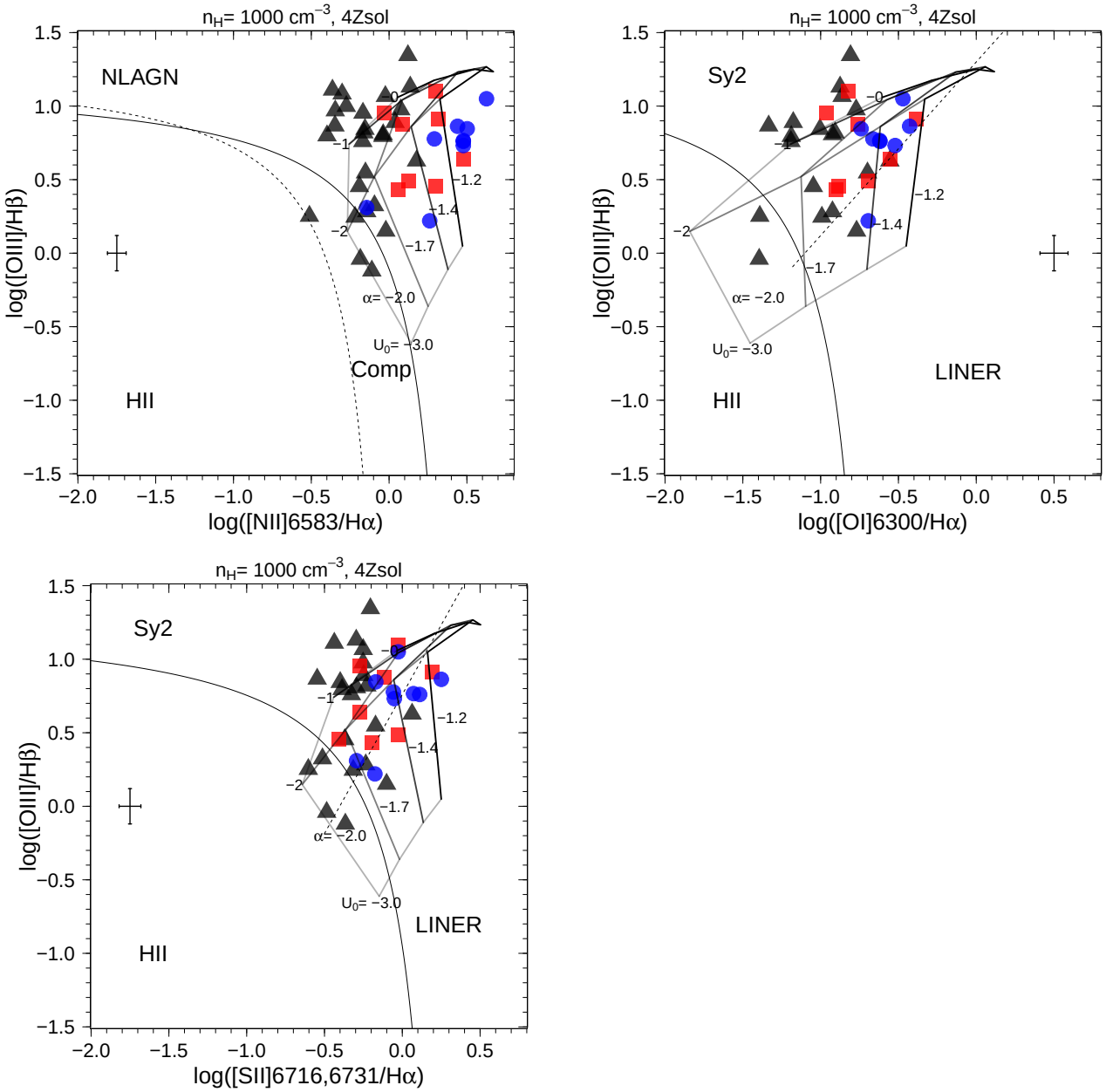


Fig. 6 Standard optical diagnostic diagrams showing the classification scheme of Kewley et al. (2006). The solid curves are the theoretical "maximum starburst line" derived by Kewley et al. (2001) as an upper limit for star-forming galaxies, and the empirical boundary lines between Seyfert 2 galaxies and LINERs. The dashed curve on the [NII] diagram is the Kauffmann et al. (2003) semi-empirical lower boundary for the star forming galaxies. The Groves et al. (2004) grids of dusty, radiation pressure-dominated models are also plotted in the Figure. These grids have been generated assuming four times solar metallicity ($4Z_{\odot}$) and hydrogen density of $n_H = 1000$ cm$^{-3}$ (see the text for a justification on the selection of these parameters). Gridlines corresponding to five values of ionizing parameter ($U_0$ = 0,-1,-2,-3,-4) and four values of power law index ($F_\nu \propto \nu^\alpha$, $\alpha$ = -1. 2, -1.4, -1.7, -2.0) are shown in the figure. To help the reader follow the gridlines these are grey-coded from "light-grey" to black, with light-grey and black corresponding to the lowest and highest values of $U_0$ and $\alpha$ respectively. Over-plotted on the diagrams are the results of our kinematic study. Black triangles are the line ratios corresponding to the narrow components, red squares correspond to the intermediate component and blue circles represent the broadest kinematic components. For clarity, no individual error bars are shown in the Figure. However, to give an idea of the uncertainty associated to the line ratio measurements a cross symbol indicates the median of all line ratio errors in each respective diagram. (A color version of this Figure is available in the online journal.)

densities ($n_e$), abundances and shock velocities ($v_s$). In addition, the predicted line ratios depend on the geometry of the shock, i.e. the presence of a photoionized precursor (see Allen et al. 2008, for a detailed discussion). In this context, Dopita & Sutherland (1995) and Allen et al. (2008) found that the shock+precursor models produce a better fit to the line ratios measured for their samples of Sy2 galaxies. Furthermore, given the typical velocities associated with the ionized gas ($v > 150$ km s$^{-1}$), one would expect the photoionization front to expand and form a precursor HII region ahead of the shock (see Dopita & Sutherland 1995; Allen et al. 2008, for a detailed discussion). For this rea-

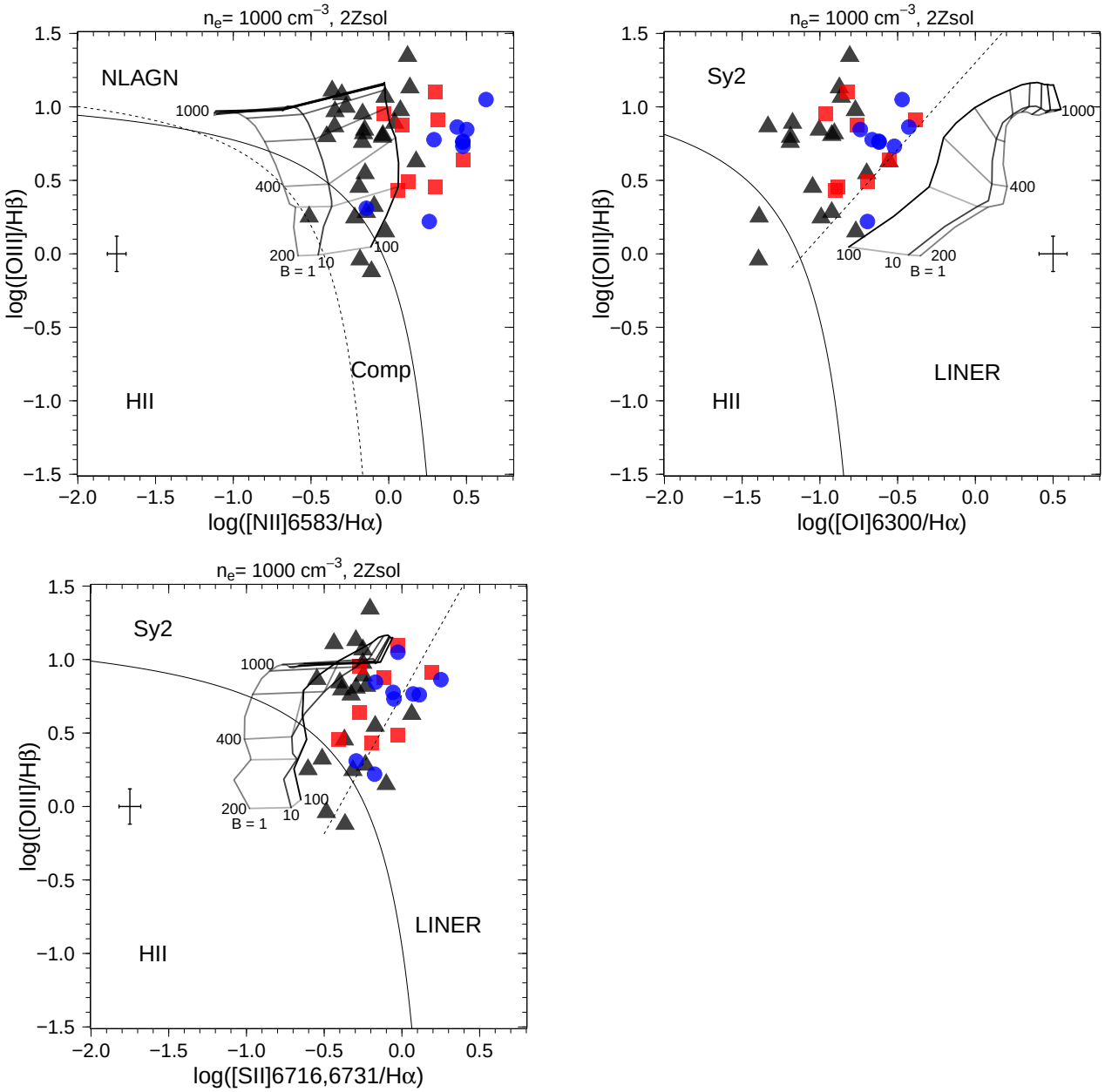


Fig. 7 Same as Figure 6 but showing the Allen et al. (2008) grids of shock-ionization models. These grids have been generated assuming a shock+precursor model with twice solar metallicity and pre-shock density of $n_e$=1000 cm$^{-3}$. Gridlines corresponding to 3 values of magnetic field ($B$ = 1, 10 and 100 $\mu$G) and 9 shock velocity values ($v_s$ = 200, 300, 400, 500, 600, 700, 800, 900 and 1000 km s$^{-1}$) are shown in the figure. $v_s$ increases always from bottom to top with 3 values (200, 400 and 1000 km s$^{-1}$) indicated in the figure. As in the case of Figure 6, the gridlines these are grey-coded from "light-grey" to black, with light-grey and black corresponding to the lowest and highest values of $B$ and $v_s$ respectively. The symbols and colors are the same as in Figure 6. (A color version of this Figure is available in the online journal.)

sons, we decided to use models with precursor for the work presented in this section.

We note that RZ13 found that, in general, shock models fail to reproduce the emission line ratios measured in the nuclear regions of the galaxies in their sample of Sy-ULIRGs, unless some extreme parameter values are used (e.g. pre-shock density of 1000 cm$^{-3}$). With this in mind, Figure 7 shows the Allen et al. (2008) models with twice solar metallicity (2Z$_\odot$) and a pre-shock density of 1000 cm$^{-3}$.

The value of the pre-shock density is one of the largest uncertainties in these models. For example, RZ13 carried out a spectroscopic study of a sample of Sy-ULIRGs and measured electron densities (n$_e$) of ∼1000 cm$^{-3}$ (although n$_e$ can be substantially higher in some extreme cases: see RZ13 for a discussion on the uncertainties associated with the electron density measurements). Assuming that these densities are associated with the compressed post-shock gas in the kinematically disturbed emission line components, then the pre-shock densities could be as low as 10 – 100 cm$^{-3}$, since the compression factor in the cooled, post-shock gas can be high (∼10-100, see Dopita & Sutherland 1995). Note that pre-shock densities of 1000cm$^{-3}$ would lead to post-shock densities of at least

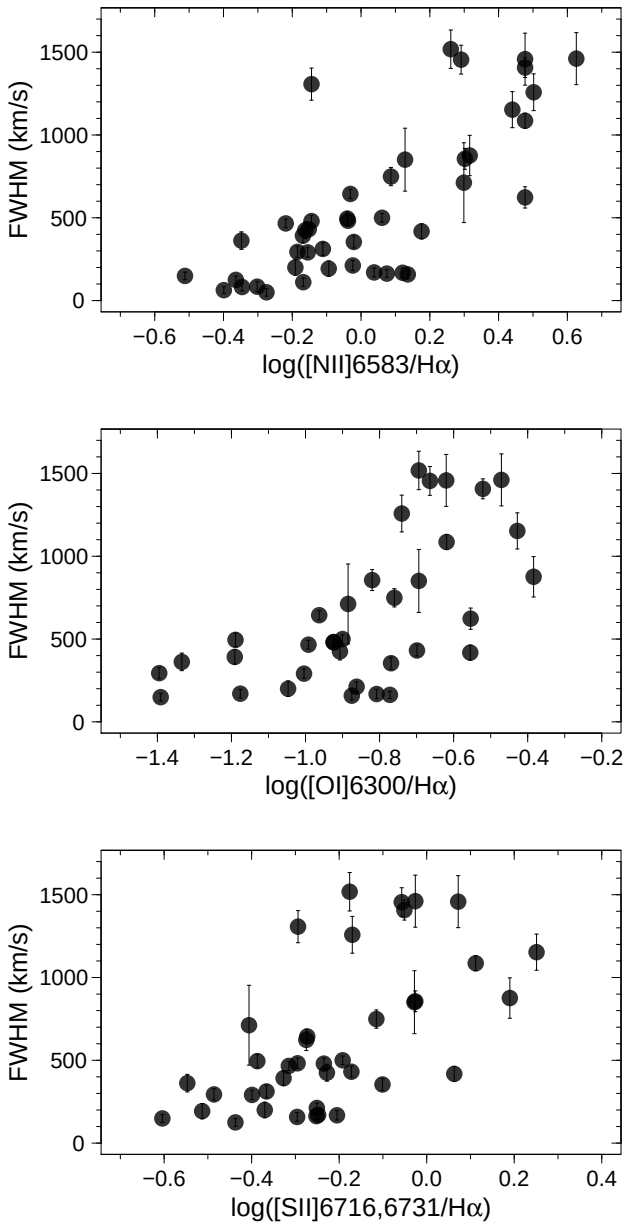


Fig. 8 Velocity widths (FWHM) of the kinematic components at the different locations in the galaxy plotted against the line ratio values.

10000 cm$^{-3}$. Therefore, a pre-shock density of 1000cm$^{-3}$ is indeed an extreme assumption.

Figure 7 shows that, even using the extreme pre-shock density of 1000 cm-3 (as assumed by RZ13), the majority of the measured line ratios do not fall within the region covered by the grids of shock models in the case of the [OIII]$\lambda$5007/H$\beta$ vs [NII]$\lambda$6583/H$\alpha$. The disagreement is even higher for the other two diagrams, where practically none of the emission lines are covered by the gridlines. As in the previous section, we have exhaustively explored the parameter space ($B$, $v_s$, $n_e$ and abundance). The agreement between the models and the measured emission lines improves when considering the extreme of $B = 1000$ $\mu$G (this is the highest $B$ value included in the Allen et al. (2008) models). However, such enormous magnetic fields are unlikely to be found in starburst galaxies (Thompson et al. 2006). Similarly, models with no precursor reproduce better the observed emission line ratios. However, as we mentioned before, given the high shock velocities indicated by the emission line kinematics, the presence of precursor HII regions ahead of the shock is expected.

Finally, it is possible to further test the importance of shock ionization in Mrk273 by investigating whether there are correlations between the emission line kinematics and the line ratios. Figure 8 shows the line widths (FWHM) of the kinematic components at the different locations in the galaxy plotted against their corresponding line ratios. Shock models predict a strong correlation between these two quantities. Therefore, these plots have been used in the past to indicate the presence of shock ionization (e.g. Armus et al. 1989; Dopita & Sutherland 1995; Veilleux et al. 1995; Monreal-Ibero et al. 2006; Rich et al. 2011). In the case of Mrk273, we find that the FWHM and line ratios are significantly correlated, with Spearman's rank correlation coefficient ($\rho$) of 0.69, 0.64, 0.63 for the [NII]/H$\alpha$, [OI]/H$\alpha$ and [SII]/H$\alpha$ plots respectively, and p-value << 0.01 for all three plots (assuming a t-distribution). However, as indicated from the $\rho$ values, the correlations are not particularly strong.

We further note that shocks may not be a unique explanation of any correlations between line width and line ratios. For example, it is possible that the emission lines in the kinematically disturbed regions were initially accelerated either by shocks or slow entrainment in an AGN-driven wind, but then photoionized by the AGN. In contrast, the more kinematically quiescent gas (with low FWHM) has not been accelerated. and is part photoionized by stars or by the AGN at higher ionization parameter (because it has a lower density due to the lack of shock acceleration). This combination of components could result in a correlation between line width and ionization state, even if the more kinematically disturbed components are currently energized by the AGN photoinization.

Overall, while the line ratios are generally more consistent with AGN photoionization than they are with shocks, the correlations that we find between the line widths and the emission line ratios suggest that shocks may contribute at some level. Further work, using fainter diagnostic emission lines including, for example, [OIII]$\lambda$4363 and HeII$\lambda$4686, will be required to determine the contribution of shocks to the line emission in the nuclear regions of Mrk273 in a definitive way.

### *4.3. Mrk273: understanding the relation between the nuclear and extended ionized gas emission*

From the results presented above, it is clear that the morphology and kinematics of the warm ionized gas in Mrk273 are extremely complex. Disturbed emission line kinematics are observed at almost all locations around the nuclear regions. Our imaging and spectroscopic results suggest that we are witnessing a variety of phenomena occurring on different scales in the galaxy. To better understand these phenomena, we concentrate here in 6 apertures that sample the main regions of interest and are representative of the diverse kinematic properties observed. These are: Ap-a, Ap-b, Ap-c, Ap-d, Ap-h and Ap-j (the modeling results for the H$\alpha$+[NII] complex for these 6 apertures are shown in Figure 4). Figure 9 shows the line ratios obtained for these par-

ticular apertures, while table 4 shows the optical spectral type derived from each line ratio diagram, and the adopted classification for each extraction aperture.

#### 4.3.1. The nuclear superbubble and the Outflow-West and Outflow-East structures

In terms of the kinematics, our results are, in general, consistent with those of Colina et al. (1999) and RV13, i.e. the kinematics in the central region of the galaxy can be described with a nuclear superbubble oriented N-S and a less collimated E-W outflow. However, the Colina et al. (1999) IFS observations have relatively low spatial and spectral resolution and the authors required only two kinematic components to model the emission lines from the galaxy at all locations. On the other hand, the RV13 observations represent a significant improvement in sensitivity, spatial and spectral resolution with respect to those of Colina et al. (1999), although their FOV does not cover most of the region with enhanced [OIII] emission to the west, and the entire [OIII] emission to the east of the nuclear region.

In this context, our new *HST* observations sample, at higher spatial resolution, the entire emission from the galaxy, while the *INT*-IDS observations provide spectroscopic information for the nuclear and extended structures (albeit with lower spatial resolution). For example, the [OIII] morphology shown in Figure 1, and the modeling results in Figures 4 and 5 allow us to place better constrain the properties of the E-W outflow. Our results suggest that Outflow-East and Outflow-West are part of the same outflow phenomenon, extending ∼4kpc from east to west at PA∼80° relative to the RV13 nuclear superbubble.

In addition, covering a wavelength range of ∼4000–7200Å, the *INT*-IDS observations allow us to study the ionization mechanisms responsible for the emission at these locations. Figure 9 and Table 4 show that the line ratios at the location of the S-Bubble are consistent with Sy2 ionization, while those corresponding to the location of N-Bubble show a mix between Sy2, LINER and HII ionization in the different BPT/VO87 diagrams. As seen in Figure 1, the S-Bubble is located closer to the SW nucleus and possibly illuminated by the AGN at that nucleus, which could explain the different line ratios relative to those of the N-Bubble.

In the case of Outflow-West region, line ratios consistent with Sy2 ionization are found for all the 3 kinematic components in the three BPT/VO87 diagrams. This result, along with the location of the region relative to the SW nucleus, clearly suggest that this region is being illuminated by the AGN in the SW nucleus of the galaxy. For Outflow-East, the line ratios show a mix of HII, LINER and Sy2-like ionization[5].

#### 4.3.2. The SE compact structure

Coinciding exactly with the location of the so-called SE nuclear component we find the brightest and most compact (FWHM = 0.14 arcsec or 106 pc, see Section 3.1) condensation of [OIII] emission in the galaxy. The nature of the SE component remains controversial. It was first identified as a star cluster based on NICMOS images (Scoville et al. 2000). Bondi et al. (2005) carried out a study of the source using milliarsecond resolution, high sensitivy radio observations. These authors found that, at radio wavelengths, the SE structure has a steep spectral index ($\alpha \simeq 1.4$) with no compact and/or flat spectrum feature (Bondi et al. 2005), and is fully resolved at 5mas resolution. However, despite the quality of their observations, the authors could not determine the nature of this nuclear component in a decisive way. On the other hand, U et al. (2013) carried out an AO-IFU study of the central kpc of the source. Their results based on the [SiVI] emission, and the [SiVI]/Br$\alpha$ line ratios, suggest that the dominant ionization mechanisms for SE component is AGN photoionization, although some contribution from shocks cannot be ruled out. Considering these results, together with the morphology of the nuclear region observed in their IFU data, U et al. (2013) proposed a scenario in which the SE component is ionized by an AGN in the N nucleus that is completely obscured along our line of sight at optical wavelengths. This raises the possibility of Mrk273 being a dual AGN.

Figure 4 shows the H$\alpha$+[NII] emission lines at the at the location of the SE component. Two kinematic components are required to provide a good fit to the emission line profiles at this location: a "narrow" component with FWHM of 431±11 km s$^{-1}$, and a broad component with FWHM = 1407±47 km s$^{-1}$ redshifted 125±28 km s$^{-1}$ relative to the narrow component. The line ratios for these two kinematic components fall in the limiting region between LINER and Sy2 ionization, and far from the HII ionization region, in the three BPT/VO87 diagrams.

To shed light on the nature of the SE compact structure it is necessary to consider both the results in this paper and those of previous studies at other wavelengths. In the first place, we further emphasize that its structure is extremely compact, and no morphological connection between this structure and the N or SW nucleus is observed in our *HST* images. In addition, strong high ionization emission lines are observed at both optical (this study) and near-IR wavelengths (U et al. 2013). Furthermore, there is significant continuum emission at this location, especially in the I, H and K bands (U et al. 2013). Together, these results strongly suggest that the SE component is a separate nucleus with its own AGN, rather than a patch of ISM illuminated by the AGN in one of the other nuclei (U et al. 2013). In this scenario the enhanced continuum emission in the red-optical and near-IR bands would represent the direct light of stars in the remnant of the bulge surrounding the putative supermassive black hole.

The only caveat associated with this scenario is the lack of a clear or X-ray or near-IR point source at the location of the SE component (Iwasawa et al. 2011). However, this can be explained if the X-ray AGN is heavily obscured by circumnuclear material, even at near-IR wavelengths, so that we are seeing the NLR of the AGN rather than the AGN continuum directly. It is also possible that the AGN at the SE nucleus has an intrinsically lower luminosity that the AGN at the SW (and N?) component. Perhaps the NLR and any stellar component associated with the SE nucleus are less obscured that those of the other nuclei and therefore, appear stronger at optical wavelengths.

[5] The narrowest component (FWHM = 193±29 km s$^{-1}$) makes a negligible contribution to the [OI] emission within this extraction aperture (Ap-d). Therefore, this component is not required to adequately model the [OI] emission line profile (i.e., if included, its properties are entirely unconstrained). Hence, no [OI]/H$\alpha$ line ratio is shown in the corresponding line ratio diagram in Figure 9.

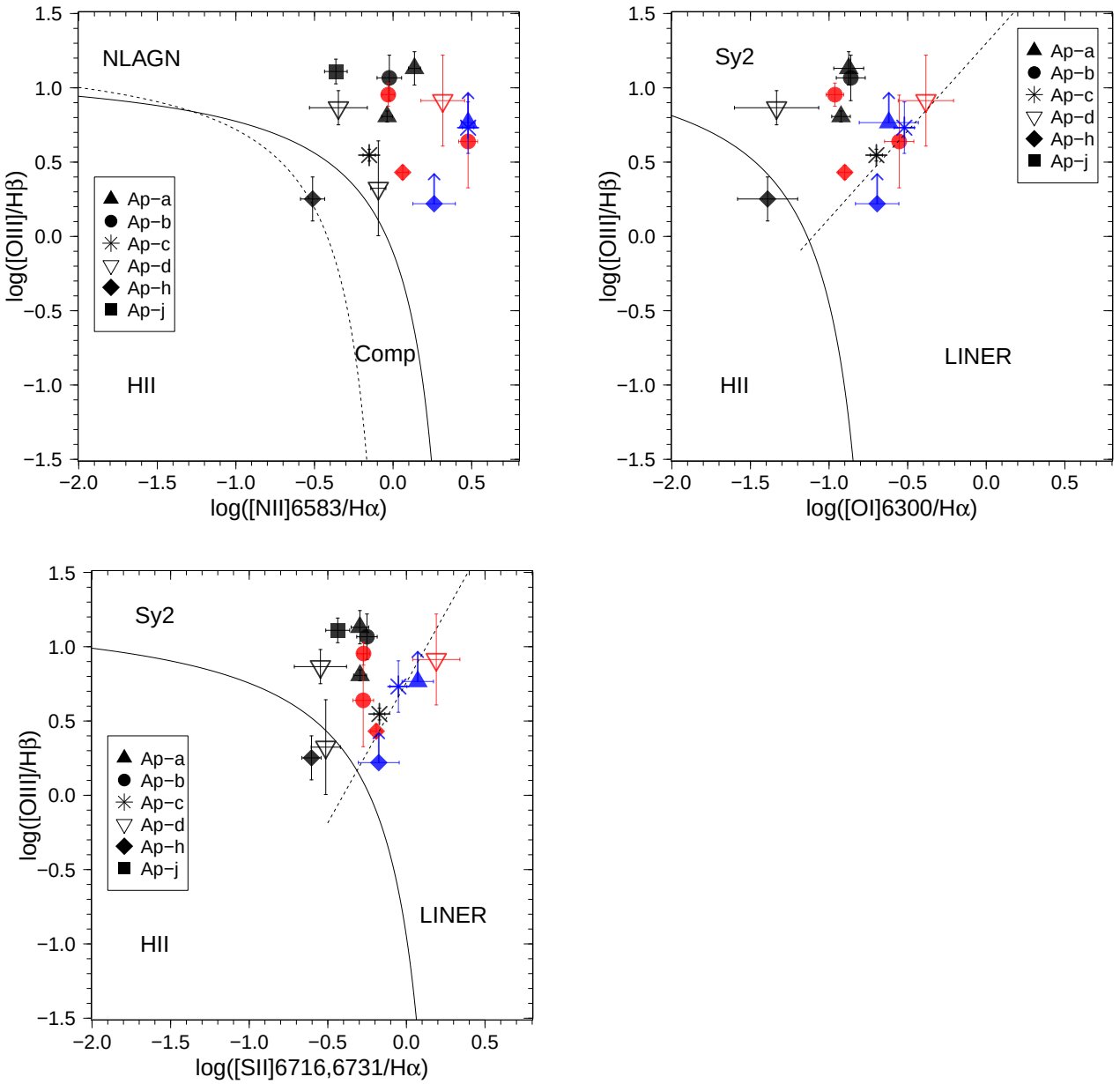


Fig. 9 Same as Figure 6 but for the 6 apertures covering the main regions of interest in Mrk273 (see the text for details). The symbols correspond to the different apertures and are indicated in the figure, while the colors code the FWHM range: black, red and blue correspond to narrow, intermediate and broad kinematic components respectively. (A color version of this Figure is available in the online journal.)

Overall, our results are consistent with the idea that the SE component is a separate nucleus with a strongly obscured, and perhaps relatively low luminosity, AGN. However, there are some caveats associated with this scenario, and further observations are required to help elucidate the nature of this compact structure.

#### 4.3.3. The extended filaments

The most spectacular features observed in the *HST*-[OIII] and the *INT*-H$\alpha$ images of the galaxy are the filaments and clumps of ionized gas emission extended $\sim$30 arcsec ($\sim$23 kpc) to the east of the nuclear region. Interestingly, the kinematics at all locations in these filaments covered by our slits are drastically different from those in the nuclear regions, with no signs of multiple kinematic components. In fact, a kinematic model comprising a very narrow component (FWHM $\lesssim$ 100 km s$^{-1}$) in sufficient to model the emission lines from the extended filaments. In addition, our kinematic results suggest the presence of a positive velocity gradient across the structure, with velocity shifts increasing from $\Delta$V of -77$\pm$24 km s$^{-1}$ relative to the rest frame in the inner regions to 114$\pm$27 km s$^{-1}$ in the outer regions.

Regarding the ionization mechanisms, for all locations across the extended filaments the line ratios fall within the Sy 2 ionization region of the 3 BPT/VO87 diagrams shown in Figure 9. Note that, since only one kinematic component is required to model the emission lines, the degener-

| Aperture | Region | Comp | BPT/VO87 | | | Class |
|---|---|---|---|---|---|---|
| | | | [NII]/H$\alpha$ | [OI]/H$\alpha$ | [SII]/H$\alpha$ | |
| (1) | (2) | (3) | (4) | (5) | (6) | (7) |
| Ap-a$^\star$ | Outflow-W | N1 | S2 | S2 | S2 | S2 |
| | | N2 | S2 | S2 | S2 | S2 |
| | | B | S2 | S2 | L/S2 | S2: |
| Ap-d | Outflow-E | N1 | S2/H | ... | H/S2 | Cp |
| | | N2 | S2 | S2 | S2 | S2 |
| | | I | S2 | S2/L | L/S2 | Cp |
| Ap-b | Bubble count | N | S2 | S2 | S2 | S2 |
| | | I1 | S2 | S2 | S2 | S2 |
| | | I2 | S2 | S2/L | S2 | S2: |
| Ap-h$^\star$ | N-Bubble | N | H/Comp | H/S2 | H | Cp |
| | | I | S2 | S2 | S2/L | S2: |
| | | B | S2 | L/S2 | L/S2 | Cp |
| Ap-c | SE compact | N | S2 | S2/L | S2/L | Cp |
| | | B | S2 | S2/L | S2/L | Cp |
| Ap-j | Ext. filaments | N | S2 | S2 | S2 | S2 |

Table 4 Line ratios measured for the different apertures/regions and for the different kinematic components. Col (1): extraction aperture. Col (2): corresponding region covered by the extraction aperture. Col (3): kinematic component. Col (4)-(6): the optical spectral type for each of the diagnostic diagrams. The symbols are: H = HII galaxies, L = LINER and Sy2 = Seyfert 2. Col (7): adopted optical spectral type. Cp indicates a mix between S2 and LINER and/or HII spectral types. Following Yuan et al. (2010) notation, single colons indicate apertures with the same spectral classification in two of the diagnostic diagrams.
$^\star$ For the broad component in these two apertures we assumed an H$\alpha$ to H$\beta$ ratio of 3. Therefore, the [OIII]/H$\beta$ line ratios calculated are lower limits of the real values.

acy issues do not affect the modeling results in this case. In addition, the continuum emission associated with this structure is relatively weak. Therefore, the line ratios measured for the ionized gas emission in the extended filaments and clumps are extremely reliable.

It is interesting to consider how this extended structure might have formed. In the first place, it is well known that major galaxy mergers are violent events, with a duration of up to few Gyrs from the first encounter to the time when the two nuclei finally coalesce (e.g. Mihos & Hernquist 1996; Barnes 2004; Springel et al. 2005; Cox et al. 2008; Johansson et al. 2009). Numerical simulations show that, at various stages during the merger event, the gas rains down into the central regions of the merging galaxies triggering star formation, and possibly, AGN activity (e.g. Springel et al. 2005; Cox et al. 2006; Hopkins & Elvis 2010). This generates outflows that, intermittently, blow out material from the central regions to larger scales (e.g. Hopkins et al. 2005; Springel et al. 2005; Cox et al. 2006). As the merger event progresses, the high expansion velocity of the material ejected at early stages gradually decreases due to gravitational effects. Part of this material will eventually escape from the potential well of the merging system into the IGM, while the fraction that remains gravitationally bound is accreted again onto the central region.

In this context, Mrk273 is a merger in its late stages, where the two (or three) nuclei are close to coalesce. The [OIII] emission from the extended structure show a bubble-like morphology that, at first sight, suggests that the gas has been blown out from the nuclear region. Therefore, it is possible that the emission in the extended filaments is associated with an outflow induced by AGN-activity at early stages in the merger. In this scenario, the gas in the filaments has progressively slowed down and any turbulence has partially dissipated, which would partially explain the emission line properties at these locations.

Another possibility is that the extended filaments are related to a more recent outflow event, with the gas in the filaments rapidly expanding in the galaxy almost perpendicular to the line of sight. In this case, he quiescent kinematics of the extended emission would be explained in terms of projection effects. However, if the ionized gas emission in the extended filaments is really due to outflows (either induced by past AGN activity or related with a more recent event), one would expect the emission lines from the extended filaments to show at least some evidence for broadening, due to turbulence in the outflow. As we described before, we find no evidence for complex kinematics, and the ionized gas in the extended filament is extremely quiescent (i.e. very narrow FWHM). Certainly these results do not favour a scenario in which the gas in the extended filaments is related to an outflow event.

Furthermore, our continuum image, as well as previous broad-band continuum (or continuum dominated) images from the ground (Mazzarella & Boroson 1993; Hibbard & Yun 1996; Kim et al. 2002) and the *HST* (GO 10592, PI: Aaron Evans) show significant continuum emission at the locations of the extended filaments. Such emission is likely to trace the starlight. However, it seems unlikely that stars would be able to form in the extreme conditions of an outflow (but see Tadhunter et al. 2014 and Zubovas & King 2014). Therefore, considering all these results, we favour a scenario in which the entire ionized gas emission from the filaments and clumps represents tidal debris left over from a secondary merger event that is illuminated by one of the AGNs in the galaxy. This would be consistent with the quiescent kinematics of the extended filaments, the Sy2 ionization line ratios and also the presence of continuum emission, due to stars from one of the precursor galaxies than now form part of the tidal debris. Note that this scenario resembles that described by McDowell et al. (2003) for Arp220. In that paper, the authors found that "lobes" of

extended, faint, edge-brightened ionized gas emission were likely related to the merger dynamics rather than the result of an outflow. Therefore, it is possible that such low surface brightness features are common among these types of merger remnants, but have so far been difficult to detect.

In terms of the relationship between the extended filaments and the nuclear structures, the morphology of the emission from the filaments closer to the nuclear region suggest that they emerge from the N nucleus. This is an interesting result since, as we mentioned before, the line ratios at all location in the filaments are consistent with Sy2 ionization. However, to date, there is no direct evidence for the presence of an AGN in that nucleus. At this stage it is worth remembering that the N nucleus is embedded in a massive rotating disk of molecular gas at PA = 70°–90° (Downes & Solomon 1998; Cole et al. 1999). Therefore, it is possible that the AGN in that nucleus is too heavily obscured to be detected in the current optical and infrared observations of the source. In addition, it is unlikely that any putative AGN within that disk illuminates the entire [OIII] nebula, as the disk would absorb the radiation along the major axis. In this context, it is possible that the extended filaments are tidal debris from the galaxy that hosted the N nucleus, but are illuminated by the AGN at the SW (or the SE) component. A second possibility is that he AGN at the N nucleus has temporarily switched off so that the extended emission from the filaments represents a "light echo", reflecting a previous phase of AGN activity.

Clearly, further observations are required to investigate the origin of the extended filamentary structure and its relationship with the nuclear structures. For example, large FOV, deep IFS observations covering the full extent of the filaments would help to distinguish between the possible scenarios described in this section for the origin of this structure. In addition, they would be extremely useful to investigate in detail which of the nuclear structures is directly related to the extended filaments.

## 5. Summary

We have used ACs/HST and INT/WFC observations to carry out an optical imaging and spectroscopic study of the warm, ionized gas in the nuclear and extended regions of Mrk273. The results from this study show that the emission line kinematics in this galaxy are extremely complex, with multiple outflows occurring in the nuclear regions of the galaxy out to a radial distance of 4kpc from the N nucleus. In addition, we find emission line ratios that are consistent with AGN photoionization as the dominant ionizing mechanism at most locations in the galaxy sampled by our slit. Shocks may also be present, but our results suggest that are not the dominant source of ionization. To gain a better idea of the physical processes ongoing in Mrk273 we have concentrated on 6 extraction apertures that sample the main regions of interest, and have investigated in detail their kinematics and ionization mechanisms. The results can be summarised as follows.

- **The nuclear superbubbles**: the presence of nuclear superbubbles oriented N-S was reported by RV13. Our *HST* [OIII] image of the galaxy shows a "U-shaped" structure to the north of the nuclear region that traces well the northern bubble (N Bubble). The Southern bubble (S Bubble) is not visible in our ACS image; this can be explained in terms of reddening effects. The kinematics measured at the locations of the bubbles are consistent with those measured by RV13, and are the most extreme in the galaxy. The line ratios indicate a mix between HII, LINER and Sy2 mechanisms for N-Bubble, while S-Bubble has line ratios typical of Sy2 ionization for all the kinematic components. These results are consistent with the nuclear superbubbles emerging from the N nucleus of the galaxy. The proximity of S-Bubble to the SW nucleus could explain the different line ratios between the two sides of the bubbles. Of course, another possibility is that the line ratios in S-Bubble are directly related to an AGN buried the N nucleus.
- **Outflow-West and Outflow-East**: Three kinematic components are required to model the emission from both Outflow-West and Outflow-East. In the case of Outflow-West, emission line ratios consistent with Sy2 ionization are found for the 3 kinematic components in the three BPT/VO87 diagrams. These results, along with the location of the Outflow-West in the galaxy clearly suggest that this region is being illuminated by the AGN in the SW nucleus. For Outflow-East the line ratios show a mix between HII, LINER and dominant Sy2 ionization. Our results suggest that Outflow-East is related to Outflow-West and that the two structures correspond to a nuclear outflow expanding from west to east almost perpendicular to the nuclear superbubbles.
- **The SE compact structure**: coinciding with the location of the so called SE nuclear component, this is the brightest and most compact structure observed in the *HST* [OIII] image of the galaxy. The compact nature of this structure, the high ionization state derived from our optical study and the near-IR study of U et al. (2013), and the presence of significant continuum emission at this location in the I, H and K bands (U et al. 2013) together strongly suggests that the SE component is a separate nucleus with its own AGN rather than a clump of ionized gas illuminated by one of the other AGNs, as proposed by U et al. (2013).
- **The extended filaments**: the ACS-[OIII] and *INT*-H$\alpha$ images of the galaxy show show a spectacular system of filaments and knots of emission extending $\sim$23 kpc to the east of the nuclear region. A kinematic model comprising a a single, narrow Gaussian component provides a good fit to the emission lines, and the lines ratios are consistent with Sy2 ionization, at all locations in the filament system. These results suggest that the gas emission in the filaments is associated with tidal debris left over from a secondary merger event, with the filaments ionized by an AGN in the nuclear regions of the galaxy. Indeed, it is possible that that Outflow-West, Outflow-East and the extended filaments represent ionization cones emerging from one of the nuclei.

Mrk273 is a nearby ULIRG with a variety of interesting phenomena occurring at all scales in the galaxy. Therefore, it offers a perfect opportunity to investigate the physical processes that govern the relationship between the nuclear activity and the surrounding ISM in gas-rich mergers. The new *HST* images reveal a very disturbed morphology in the nuclear region of the galaxy, and a spectacular filamentary structure extending $\sim$23kpc to the east of the galaxy whose origin remains uncertain. In addition, we have identified the brightest and the most compact structure in [OIII] emission

with the SE component. Our results suggest that this component is a nucleus itself, with its own AGN. If this result is confirmed, as well as those of U et al. (2013) which suggest the presence of an AGN in the N disk, three AGN could potentially be co-existing in the nuclear region of Mrk273.

Overall, these results demonstrate the potential of deep observations of the extended emission line gas for unravelling the complexity of ULIRGs, determining the nature of triggering mergers, and the gauging the importance of feedback effects associated with their AGN.

## Acknowledgments

JRZ and CRA acknowledge financial support from the spanish grant AYA2010_21887-C04-04. The Isaac Newton Telescope is operated on the island of La Palma by the Isaac Newton Group in the Spanish Observatorio del Roque de los Muchachos of the Instituto de Astrofisica de Canarias. JRZ would like to thank Manuel Díaz Alfaro and Javier Piqueras López for the help with the R and IDL codes used in this paper. This research is supported in part by STFC grant St/J001589/1 and a Marie Curie IEF within the 7th European community framework programme (PIEF-GA-2012-327934).

## References

Allen, M. G., Groves, B. A., Dopita, M. A., Sutherland, R. S., & Kewley, L. J. 2008, ApJS, 178, 20
Armus, L., Charmandaris, V., Bernard-Salas, J., et al. 2007, ApJ, 656, 148
Armus, L., Heckman, T. M., & Miley, G. K. 1989, ApJ, 347, 727
Baldwin, J. A., Phillips, M. M., & Terlevich, R. 1981, PASP, 93, 5
Barber, C. R., Roberts, T. P., & Warwick, R. S. 1996, MNRAS, 282, 157
Barnes, J. 2004, MNRAS, 350, 798
Bedregal, A. G., Colina, L., Alonso-Herrero, A., & Arribas, S. 2009, ApJ, 698, 1852
Benson, A. J., Bower, R. G., Frenk, C. S., et al. 2003, ApJ, 599, 38
Bondi, M., Pérez-Torres, M.-A., Dallacasa, D., & Muxlow, T. W. B. 2005, MNRAS, 361, 748
Carilli, C. & Taylor, G. 2000, ApJ, 532, L95
Cicone, C., Feruglio, C., Maiolino, R., et al. 2012, A&A, 543, A99
Cicone, C., Maiolino, R., Sturm, E., et al. 2013, ArXiv e-prints
Clements, D. L., Sutherland, W. J., McMahon, R. G., & Saunders, W. 1996, MNRAS, 279, 477
Cole, G., Pedlar, A., Holloway, A., & Mundell, C. 1999, MNRAS, 310, 1033
Colina, L., Arribas, S., & Borne, K. D. 1999, ApJ, 527, L13
Condon, J., Huang, Z.-P., Yin, Q., & Thuan, T. 1991, ApJ, 378, 65
Cox, T. J., Jonsson, P., Primack, J. R., & Somerville, R. S. 2006, MNRAS, 373, 1013
Cox, T. J., Jonsson, P., Somerville, R. S., Primack, J. R., & Dekel, A. 2008, MNRAS, 384, 386
di Matteo, T., Springel, V., & Hernquist, L. 2005, Nature, 433, 604
Dopita, M. A. & Sutherland, R. S. 1995, ApJ, 455, 468
Dopita, M. A. & Sutherland, R. S. 1996, ApJS, 102, 161
Downes, D. & Solomon, P. 1998, ApJ, 507, 615
Fabian, A. C. 1999, MNRAS, 308, L39
Feruglio, C., Maiolino, R., Piconcelli, E., et al. 2010, A&A, 518, L155
Fischer, J., Sturm, E., González-Alfonso, E., et al. 2010, A&A, 518, L41
Genzel, R. Lutz, D., Sturm, E., Egami, E., et al. 1998, ApJ, 498, 579
Groves, B. A., Dopita, M. A., & Sutherland, R. S. 2004, ApJS, 153, 9
Hibbard, J. E. & Yun, M. S. 1996, in Astrophysics and Space Science Library, Vol. 206, Cold Gas at High Redshift, ed. M. N. Bremer & N. Malcolm, 47
Hopkins, P. F. & Elvis, M. 2010, MNRAS, 401, 7
Hopkins, P. F., Hernquist, L., Cox, T. J., et al. 2005, ApJ, 630, 705
Howell, J. H., Armus, L., Mazzarella, J. M., et al. 2010, ApJ, 715, 572
Iwasawa, K., Mazzarella, J. M., Surace, J. A., et al. 2011, A&A, 528, A137
Johansson, P. H., Burkert, A., & Naab, T. 2009, ApJL, 707, L184
Kauffmann, G., Heckman, T. M., Tremonti, C., et al. 2003, MNRAS, 346, 1055
Kewley, L. J., Groves, B., Kauffmann, G., & Heckman, T. 2006, MNRAS, 372, 961
Kewley, L. J., Heisler, C. A., Dopita, M. A., & Lumsden, S. 2001, ApJS, 132, 37
Kim, D. C., Veilleux, S., & Sanders, D. B. 2002, ApJ, 143, 277
Knapen, J., Laine, S., Yates, J.A. Robinson, A., et al. 1997, ApJ, 490, L29
Majewski, S., Hereld, M., Koo, D., Illingworth, G., & Heckman, T. 1993, ApJ, 403, 125
Markwardt, C. B. 2009, in Astronomical Society of the Pacific Conference Series, Vol. 411, Astronomical Data Analysis Software and Systems XVIII, ed. D. A. Bohlender, D. Durand, & P. Dowler, 251
Mazzarella, J. M. & Boroson, T. A. 1993, ApJS, 85, 27
McDowell, J. C., Clements, D. L., Lamb, S. A., et al. 2003, ApJ, 591, 154
Mihos, J. & Hernquist, L. 1996, ApJ, 464, 641
Monreal-Ibero, A., Arribas, S., & Colina, L. 2006, ApJ, 637, 138
Murphy, Jr., T. W., Armus, L., Matthews, K., et al. 1996, AJ, 111, 1025
Osterbrock, D., Fulbright, J., Keane, M., & Trager, S. 1996, PASP, 108, 277
Rich, J. A., Kewley, L. J., & Dopita, M. A. 2011, ApJ, 734, 87
Rodríguez Zaurín, J., Tadhunter, C. N., & González Delgado, R. M. 2009, MNRAS, 400, 1139
Rodríguez Zaurín, J., Tadhunter, C. N., & González Delgado, R. M. 2010, MNRAS, 403, 1317
Rodríguez Zaurín, J., Tadhunter, C. N., Rose, M., & Holt, J. 2013, MNRAS, 432, 138
Rupke, D. S. N. & Veilleux, S. 2011, ApJL, 729, L27
Rupke, D. S. N. & Veilleux, S. 2013a, ApJ, 775, L15
Rupke, D. S. N. & Veilleux, S. 2013b, ApJ, 768, 75
Sanders, D. B. & Mirabel, I. F. 1996, ARA&A, 34, 749
Scoville, N. Z., Evans, A. S., Thompson, R., et al. 2000, ApJ, 119, 991
Silk, J. & Rees, M. J. 1998, A&A, 331, L1
Soifer, B., Neugebauer, G., Matthews, K., et al. 2000, AJ, 119, 509
Spoon, H. W. W., Farrah, D., Lebouteiller, V., et al. 2013, ApJ, 775, 127
Springel, V., Di Mateo, T., & Hernquist, L. 2005, MNRAS, 361, 776
Sturm, E., González-Alfonso, E., Veilleux, S., et al. 2011, ApJL, 733, L16
Surace, J. A. & Sanders, D. B. 2000, AJ, 120, 604
Surace, J. A., Sanders, D. B., & Evans, A. S. 2000, ApJ, 529, 170
Thompson, T. A., Quataert, E., Waxman, E., Murray, N., & Martin, C. L. 2006, ApJ, 645, 186
U, V., Medling, A., Sanders, D., et al. 2013, ApJ, 775, 115
Veilleux, S., Kim, D. C., Mazzarella, J. M., & Soifer, B. T. 1995, ApJ, 98, 171
Veilleux, S., Kim, D. C., & Sanders, D. B. 2002, ApJ, 143, 315
Veilleux, S., Melendez, M., Sturm, E., et al. 2013, ApJ, in press
Veilleux, S. & Osterbrock, D. E. 1987, ApJS, 63, 295
Veilleux, S., Rupke, D. S. N., Kim, D.-C., et al. 2009, ApJS, 182, 628
Westmoquette, M. S., Clements, D. L., Bendo, G. J., & Khan, S. A. 2012, MNRAS, 424, 416
Yuan, T.-T., Kewley, L. J., & Sanders, D. B. 2010, ApJ, 709, 884
Zubovas, K. & King, A. 2014, ArXiv e-prints